



Influences of Slope Angle on Propagation and Deposition of Laboratory Landslides

Yan-Bin Wu^{1,2}, Zhao Duan^{2,3*}, Jian-Bing Peng^{4,5}, Qing Zhang^{1,2}

¹ Graduate Student, College of Geology and Environment, Xi'an University of Science and Technology, Xi'an 710054, China.

5 ² Institute of Ecological Environment Restoration in Mine Areas of West China, Xi'an University of Science and Technology, Xi'an, 710054, China.

³ Associate Professor, College of Geology and Environment, Xi'an University of Science and Technology, Xi'an 710054, China.

⁴ School of geology engineering and Geomatics, Chang'an University, Xi'an 710054, China.

10 ⁵ Key Laboratory of western Mineral Resources and Geological Engineering of Ministry of Education, Chang'an University, Xi'an 710054, China.

Corresponding author: Zhao Duan (duanzhao@xust.edu.cn)

Abstract

Slope angle is an important influence on the motion characteristics and deposit morphologies of landslides. In this study, an advanced 3D scanner was used to study laboratory landslides at various slope angles. The laboratory landslides had different motion characteristics. An increase of the runout of the laboratory landslides with the slope angles meant that the amount of energy loss was great due to the collision of sliding mass at the slope break. The length and area of these laboratory landslides increased first and then decreased during their whole motion. The surface morphologies of the deposits differed according to the slope angles. At low slope angles, they exhibited a series of transverse ridges formed by overthrusting. At moderate slope angles, they exhibited conjugate troughs (X-shape wash) formed by shearing on the accumulation zone. At high slope angles, they exhibited a double-upheaval morphology formed by the rear portion of the sliding mass impacting the forward portion. A theoretical relationship between the apparent friction coefficient and slope angle is proposed, based on a hypothesis the ratio of energy dissipation occurring when an object collides with a plane is exponentially related to the acute angle between the object's direction and the plane's normal direction. The study will support studies on the morphological variation during the whole motion and mobility of landslides.

25 1 Introduction

Landslides are often highly destructive due to their high mobility, especially when the landslides are with flow characteristics. Field investigations used for statistics and physical modelling experiments are common approaches adopted by researchers of landslides. Although field investigations used for statistics have advantages of in-situ observations of landslides, the actual environment of each landslide may be different. Correspondingly, the factors that affect the characteristics of landslides, such as slope angle, slope height, volume and material attributes, may be different. Therefore, it is difficult to study one of these factors to the influence to landslides. Physical modelling experiments are often employed to study different factors to the influence of the motion process and deposit morphology of landslides, and have become a research focus in recent years. Furthermore, physical modelling experiments allow the boundary conditions to be simplified and can ideally simulate the motion path and fluidization properties of natural landslides.



35 It is difficult to observe landslides in motion by field investigation. Therefore, most researchers have studied their deposit
morphology to indirectly infer the movement processes and force characteristics (Parise, 2003; Petley, 2013; Wang et al., 2018b).
Transverse ridges perpendicular to the direction of a landslide's motion are common features of the deposit morphology and are
regarded as compression-related (Crosta et al., 2017; Wang et al., 2018b). Conjugate trough structures (a kind of surface structures
with X-shape wash) are observed on the surface of some large landslide deposits. Based on field investigations, Wang et al. (2018b)
40 proposed that these conjugate troughs are formed by the mutual effects of transport-parallel compression and radial spreading.
However, Zhao et al. (2021) suggested that their formation is closely related to the stress state of the landslide while it is moving.
The stress state is similar to the triaxial stress state, which provides a fundamental condition for the formation of conjugate troughs.
In fact, these phenomena of transverse ridges and conjugate troughs are related to the slope angle. It is noticeable that previous
explanations on the formation of conjugate troughs are from field investigations and lack of experimental analysis. Therefore, the
45 reason for the formation of the conjugate troughs and how the motion process of sliding masses affects the formation should be
explored in-depth based on physical model experiments.

Landslides sliding down slopes of different angles have different motion characteristics. The Luanshibao landslide in the
Tibetan Plateau, China, had a sliding distance of 3910 m, an apparent friction coefficient of 0.207, a slope angle of 45° and a height
of 830 m (Dai et al., 2019; Zeng et al., 2019). According to investigations of chalk flows in the southern coast of Europe
50 (Hutchinson, 2002) and landslides in the Fukushima open pit area in Japan (Whittall et al., 2016), at high slope angles (> 60°), the
runout is relatively low and, correspondingly, the apparent friction coefficient is larger. Of course, the difference in the apparent
friction coefficients of these landslides is not only caused by differences in slope angle but also by differences in volume and the
type of sliding mass. However, the slope angle has a more significant effect on the apparent friction coefficient (Duan et al., 2020;
Huang and Liu, 2009).

55 Although slope angle is an important influence on the motion of landslides, there are few studies on this effect (Duan et
al., 2020). However, some researchers have used physical modelling experiments to carry out related research. Fan et al. (2016)
used flume experiments to study the kinetic parameters (displacement, velocity, and acceleration) and energy dissipation modes of
laboratory landslides at slope angles of 25–55°. They concluded that energy dissipation increases with slope angle. Crosta et al.
(2017) performed physical modelling experiments with no sidewall constraint to study the impact dynamics and modes of
60 laboratory landslide deposition at slope angles of 40–65°. However, due to the limited range of slope angles considered, the studies
by Fan et al. (2016) and by Crosta et al. (2017) do not reflect the motion characteristics of laboratory landslides at high slope angles.
Although Roche et al. (2021) conducted chute experiments with a wide range of slope angles from 13.4° to 83.6°, they mainly
focused on the variation in effective basal friction coefficient (the ratio of the force along the sliding mass direction to the that in
the normal direction) with slope angle. The motion characteristics and deposit morphologies of sliding masses were not considered.
65 As a consequence, researches on the corresponding relation between the motion characteristics and deposit morphologies of sliding
masses should be conducted forward under a larger various range of slope angles.

The dynamics and friction laws of granular flows sliding down from an inclined plate were extensively studied in past
few decades (Lucas et al., 2014; Baker et al., 2016; Pirulli et al., 2007; Mangeney et al., 2007b; Lusso et al., 2017; Edwards and
Gray, 2015; Edwards et al., 2021; Edwards et al., 2017; Gray et al., 1999). The methods to study the dynamics and friction laws
70 of granular flows are the numerical simulation, theoretical deduction, and physical model experiments. The theoretical deduction
to issues of granular motion is a fundamental means to provide model laws to the numerical simulation methods. The numerical
simulation been employed to perform numerical experiments is often used to validate a theoretical analysis when a modified motion
law or friction law is proposed to granular materials during motion (Farin et al., 2014). Nevertheless, the physical model



75 experiments are constantly supplying thoughts to theoretical and numerical methods, such as the experimental phenomena of
erosion-deposition waves (Edwards and Gray, 2015; Edwards et al., 2021; Farin et al., 2014; Mangeney et al., 2010a), formation
of levees and troughs (Baker et al., 2016; Edwards et al., 2017), and particle size-segregation (Baker et al., 2016). For physical
model experiments, the setups of an experiment are a critical influence for the experimental results. Gray et al. (1999) performed
laboratory experiments that a shallow parabolic cross-slope topography is superposed to an inclined chute with a slope angle of
40° to confine the avalanche motion and conjoined smoothly with a horizontal plate. The contour maps during motion can reflect
80 well the avalanches' motion characteristics. Similarly, the experiments conducted by Mangeney et al. (2010a) and Farin et al.
(2014) for exploring the dynamics and erosion processes of granular flows were carried out on an inclined chute with side walls.
In their studies, a critical slope angle was proposed. The duration of the granular materials would increase significantly beyond the
critical angle. Previous contributions on the dynamics and erosion of granular materials are abundant and significant. However, it
is still unclear the differences in motion characteristics (length, width, area during motion) when granular materials flow down
85 from an inclined plate without side walls onto a horizontal plate jointed sharply with the inclined plate. The studies in regards of
morphological variations of sliding masses during the whole motion should be performed.

After determining the parameters of the topography and deposit morphology of landslides through field investigations,
researchers commonly use statistical methods to establish relationships between topographic parameters (volume and slope angle)
and runout and deposit morphology parameters (Mcdougall, 2016; Scheevel, 2017; Dufresne et al., 2021). Such statistical
90 relationships have regional limitations, which cause the results of different groups in different regions to be inconsistent (Hunter
and Fell, 2003; Whittall et al., 2016; Crosta et al., 2017; Okura et al., 2003). In contrast, on the premise of reasonable assumptions
of the relevant parameters involved in landslides, a predictive model of the mobility of landslides based on theoretical deduction
could be more reliable. Crosta et al. (2015b) proposed a theoretical formula describing the relationship between apparent friction
coefficient and slope angle based on the law of conservation of energy and an assumption of the coefficient of velocity restitution
95 (the ratio of the velocity of an object after collision to its velocity before collision). This equation can effectively describe the
relationship between the apparent friction coefficient and slope angle of actual landslides. According to an assumption proposed
by Crosta et al. (2015b), the horizontal velocity of an object consists of two components after colliding with a plane: a horizontal
component and a partial vertical component of the velocity at the moment of collision. The results of collision tests by Zhang et
al. (2015), Wang et al. (2018a), and Ji et al. (2019) indicate that the difference in velocity before and after a collision between an
100 object and a plane is related exponentially to the object's incidence angle. Therefore, which one is more suitable to predict the
mobility of landslides based on the assumption by Crosta et al. (2015b) or the experimental results by Zhang et al. (2015), Wang
et al. (2018a), and Ji et al. (2019) is still unknown and should be discussed further.

In the studies of laboratory landslides, devices used to record their motion process are often high-speed cameras (Li et al.,
2021; Lin et al., 2020; Hu et al., 2020). Work towards the design of a device that could record the three-dimensional data during
105 the motion of the laboratory landslides to realize their comprehensive process has been ongoing. Manzella and Labiouse (2008),
Moro et al. (2010), and Wei et al. (2020) introduced the Fringe Projection Method developed a decade ago to measure the deposit
shape and position of a laboratory landslide in a relatively precise manner. In recent years, a laser profilometer is more commonly
used in physical model experiments (Crosta et al., 2015a; Crosta et al., 2017). Meanwhile, laser scanners, which could collect the
point clouds of the deposit of a laboratory landslide only when the laboratory landslide stopped completely, were employed to
110 depict the Data Elevation Model (DEM) (Ge et al., 2020). However, a device that can precisely collect the point clouds and motion
characteristics of laboratory landslides during the whole motion process has not yet been used in the study of laboratory landslides.

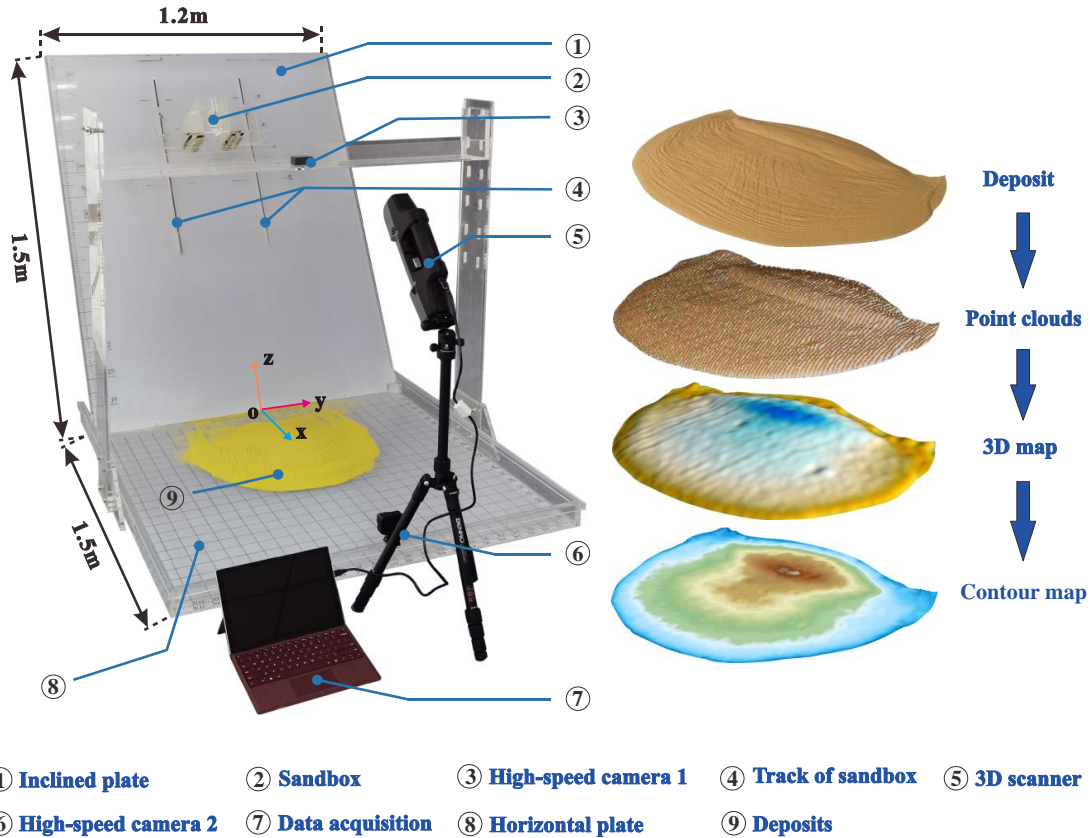


In this paper, sandbox experiments were conducted at various slope angles with a large range from 30° to 85°. During the experiments, two high-speed cameras and an advanced 3D scanner would be used to record the point clouds, images, and motion characteristics of laboratory landslides during the whole motion process. The objectives of this paper were as follows: 1) to explore variations in motion parameters and states with slope angle in the laboratory landslides; 2) to determine the influence of slope angle on deposit morphology and explain the mechanisms of deposit surface morphology and to reveal the reason for the formation of conjugate troughs from the experimental viewpoint by combining the motion process of the laboratory landslides; 3) to explore the morphological variations (length, width, and area) of the sliding masses during their whole motion; and 4) to explore the relationship between the apparent friction coefficient and slope angle based on the results of colliding experiments in physics field, and establish and verify a theoretical model of this relationship.

2 Experimental design

2.1 Experimental setup

A sandbox experiment was performed to study the motion process and deposit morphology of laboratory landslides. Plexiglass was used to construct the experimental devices, which were composed of five parts: an inclined plate, a horizontal plate, a sand container, a 3D scanner, and two high-speed cameras. A pair of sandbox tracks was set in the inclined plate to adjust the height of the sandbox. The lengths of the inclined plate and horizontal plate were 1.5 m and their widths were 1.2 m (Figure 1). A coordinate system was defined in figure 1, in which the motion direction of the laboratory landslides was the x axis direction and the z axis was perpendicular to the horizontal plate. The specified volume of the sandbox with a side-by-side gate at the bottom was $3.6 \times 10^{-3} \text{ m}^3$. A three-dimensional (3D) scanner (8 frames/s, 1.3-megapixel resolution) recorded the whole process of the laboratory landslide in motion and obtained 3D coordinate data of the upper surface. The accuracy of the 3D scanner with a model of F6 Smart produced by MANTIS VISION company was 0.1 mm. It had three lenses: an emitter lens at the bottom and two lenses at the top—one with a near-infrared (NIR) sensor and one that could acquire colour images. During scanning, an NIR ray was emitted, reflected from the surface of the objects, and received by the lenses at the top of the 3D scanner. The received NIR data were transformed into 3D cloud data and colour images. The 3D data were acquired according to the principles of stereoscopic parallax and active triangular ranging. Two high-speed cameras (120 frames/s, 0.4-megapixel resolution) were used to collect images at the end of each experiment. One was placed on a camera shelf, which could be adjusted not only up and down but also forward and backward, to obtain deposit photos with a bird view. The other one was fixed at the front of the horizontal plate with a horizontal view.



140 **Figure 1.** Apparatus used for the laboratory landslide experiments.

2.2 Materials

A medium-fine quartz sand (Figure 2) was used as the material of sliding mass in the laboratory landslides because it has a similar flow characteristic as natural landslides (Duan et al., 2019; Ma et al., 2019). Its particle-size distribution is shown in Figure 3. Its uneven coefficient $C_u = D_{60} / D_{10}$ (D_{60} denotes the particle size corresponding to the value smaller than 60% of the mass proportion, similarly D_{10} is the particle size corresponding to the value smaller than 10%.) was 2.39, the curvature coefficient $C_c = D_{50}^2 / (D_{60} D_{10})$ (D_{30} denotes the particle size corresponding to the value smaller than 30% of the mass proportion) was 1.19, and the specific surface area (the surface area per unit mass) was $0.02 \text{ m}^2 \cdot \text{kg}^{-4}$. The cumulative percentage of particles in the size range 0.075–0.42 mm was 87.71%, the average particle size was 0.18 mm. The internal friction angle φ was 36° , the cohesion c was zero, and the interface friction parameter of plexiglass and sand was 0.42. The detailed definition of the internal friction angle and cohesion was described in section 2.3 Method.

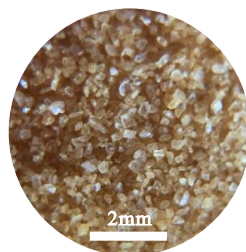


Figure 2. Photograph of the experimental material—medium-fine quartz sand.

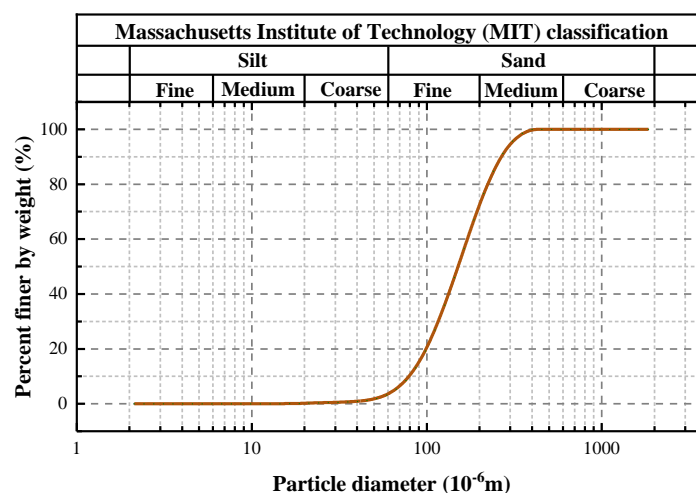


Figure 3. Particle-size distribution of the experimental material (medium-fine quartz sand).

155 2.3 Methods

We aimed to determine how slope angle affects the motion characteristics, deposit morphology, and surface structures of laboratory landslides. The centre gravity height of each experiment was kept at 0.7 m by adjusting the bracket set-back of the inclined plate with the aid of a pair of tracks (Figure 1). The volume of the sandbox was $3.6 \times 10^{-3} \text{ m}^3$, the bulk density of granular masses was $1.5 \times 10^3 \text{ kg} \cdot \text{m}^{-3}$, and the mass of sand used each time was 5.4 kg.

160 Before the formal sandbox experiments, seven groups of calibration tests were performed. The calibration tests were carried out at a slope angle of 50° , centre gravity height of 0.7 m (Figure 4), and sandbox volume of $3.6 \times 10^{-3} \text{ m}^3$. Other experimental conditions were the same as those of the formal experiments. The calibration tests aimed to quantify the systematic error in the sandbox experiments. For the formal experiments, the slope angle was taken as the independent variable and was varied from 30° to 85° at intervals of 5° . There were 12 groups of experiments in total and each group was performed at least twice. The
165 the average values of the results were used to determine the deposit morphologies and kinetic parameters of the laboratory landslides. If the difference between two deposit morphology results in a group was greater than the standard deviation obtained from the calibration tests, a third replicate was conducted. Finally, the average of the two experimental results from one group that had the minimum difference was selected to evaluate the deposit morphological parameters. During the experiments, the inclined plate, horizontal plate, and interior of the sandbox were wiped with a static-proofing liquid. After the liquid dried, the sand was filled in
170 the sandbox in three stages, with compaction and scratch carried out after the first two stages to ensure uniformity. In the last stage,



the sand was flush with sandbox by compaction. The side-by-side gate was held by a switch when the sand was put into the sandbox, then the switch was opened when the high-speed cameras and 3D scanner were operating.

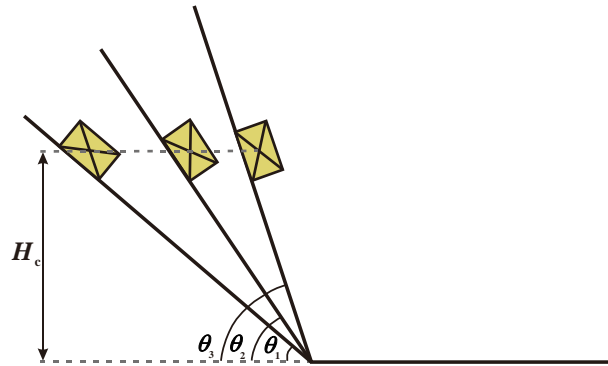
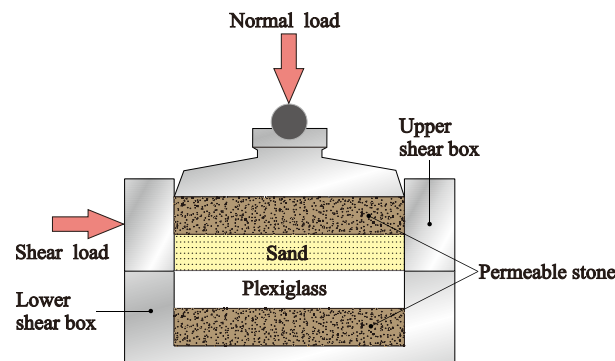


Figure 4. Variation in slope angle (H_c height of sandbox from the centre of gravity; θ slope angle).



175

Figure 5. Diagram of direct shear testing of the sand-plexiglass interface.

It was very important to determine the mechanical properties of the interface between the sand and plexiglass. In this paper, the internal friction angle of this interface was subjected to direct shear tests. The direct shear test is a fundamental method to determine the internal friction angle and cohesion of materials in the geotechnical field. The normal load can be set as different values, corresponding to which the shear load will have different values. To plot a linear fitting curve by setting the normal load as the x axis and the shear load as the y axis, the slope of the curve is the tangent value of the internal friction angle of the material. The intercept of the curve is the cohesion of the material which is 0 because the sand is non-cohesive. The tangent value of the internal friction angle, which was 0.42, was taken as the friction coefficient of the interface. When measuring the internal friction angle at the interface, a customized plexiglass block with a size of $\phi 61.8 \times 10$ mm and sand were placed into the lower and upper shear boxes, respectively, so that the contact surface between the plexiglass and sand was the shear plane (Figure 5). The upper and lower permeable stones are in order to an even load acted on the material during the shear tests. Both the upper and lower shear boxes were filled with the sand with density $1.5 \times 10^3 \text{ kg}\cdot\text{m}^{-3}$ to measure the properties of the sand.

180

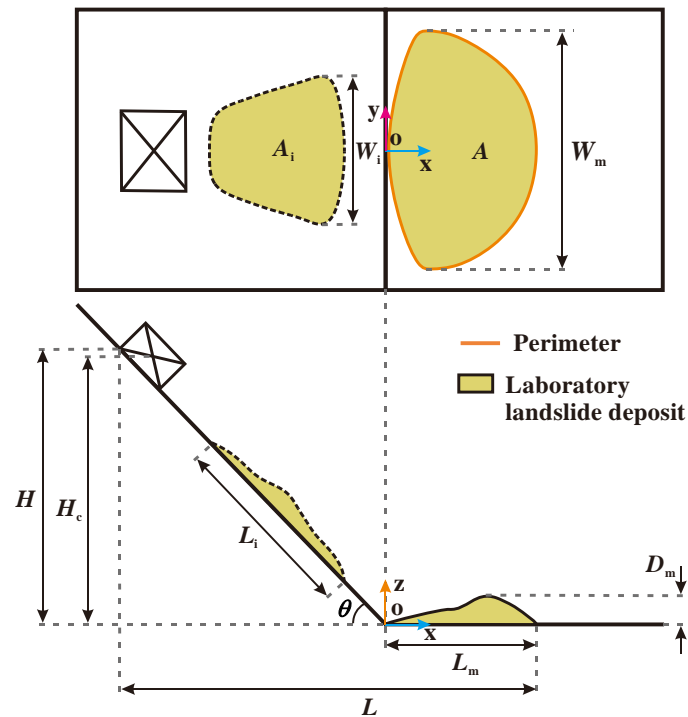
185



3 Results

3.1 Quantifying dispersion of the experiments

190 In this paper, the maximum length, maximum width, maximum depth, area, length-width ratio and perimeter-area ratio
 of the deposit were used to quantify change in the deposit morphology of the laboratory landslides (Figure 6). The deposit
 morphology results of the calibration tests are shown in Figure 7. The error bars of these six indexes of deposit morphology each
 contain a number representing the arithmetic mean. The arithmetic means of the maximum length, maximum width, maximum
 depth, area, length-width ratio and perimeter-area ratio were 474.94 mm, 701.84 mm, 37.25 mm, $24.6 \times 10^4 \text{ mm}^2$, 0.677, and 0.089,
 195 respectively. The standard deviation is often used to reflect the degree of dispersion of a measured value. In the calibration tests,
 the standard deviations of these six indexes were 3.47, 5.59, 0.71, 0.31, 0.005, and 0.001, respectively. According to the three-
 sigma rule, the measured values are within the margin of error if they are within the interval of $[\bar{x} - 3\sigma, \bar{x} + 3\sigma]$. Differences in
 the values recorded in each experiment were caused by systematic error. In the sandbox experiments, each morphological parameter
 result was considered reasonable at 99.7% confidence if it was within the interval of $[\bar{x} - 3\sigma, \bar{x} + 3\sigma]$. Changes in slope angle were
 200 expected to lead to changes in deposit morphology. Experimental results greater than the interval indicate that slope angle had a
 significant influence on deposit morphology.



205 **Figure 6.** Diagram of the deposit morphology of laboratory landslides: L_m maximum length of deposit (a projected length of the deposit from the most rear part to the front part on the x - o - y plane); W_m maximum width of deposit; D_m maximum depth of deposit; A area of deposit projected on horizontal plane; P perimeter of deposit; θ slope angle; H height of sandbox scarp to horizontal plate; H_c height of sandbox from the centre of gravity; L runout of laboratory landslides; L_i length of sliding mass during motion; W_i width of sliding mass during motion; A_i area of sliding mass during motion.

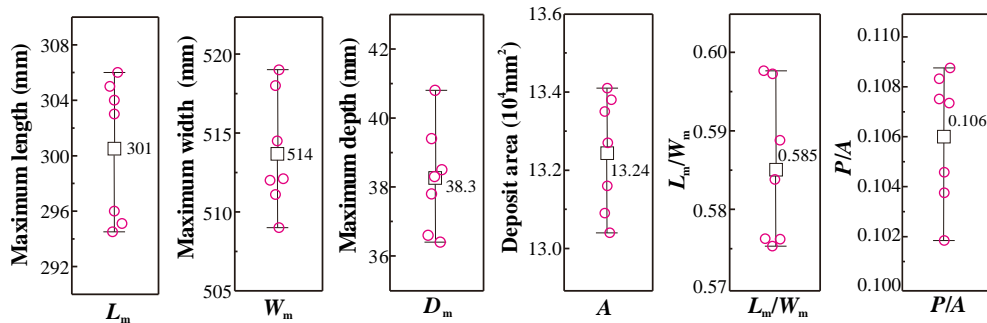
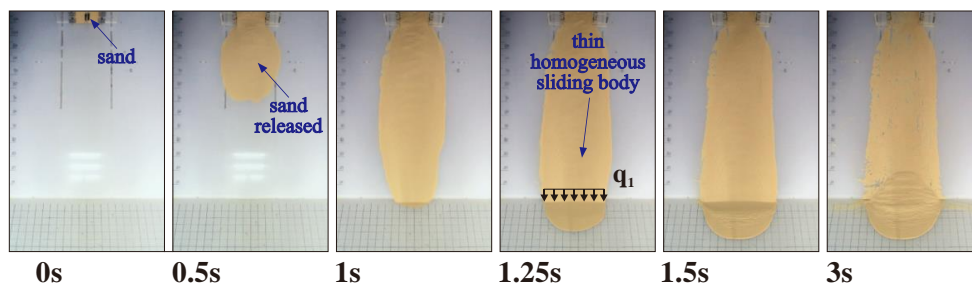


Figure 7. Results of calibration experiments.

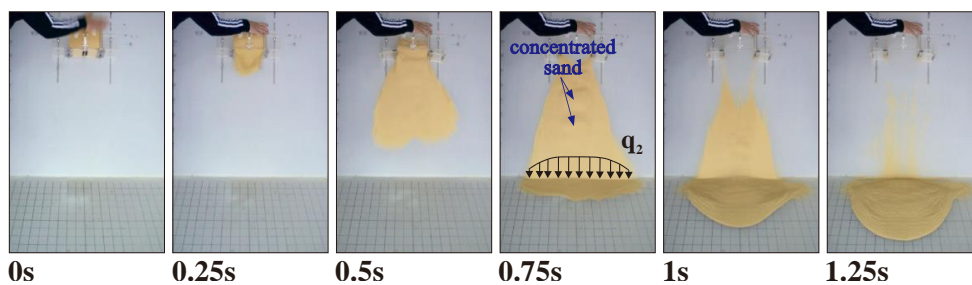
3.2 Motion characteristics

3.2.1 Motion process and runoff

The morphological characteristics during the motion of the laboratory landslides was different at different slope angles. However, they were similar in each interval of slope angles including 30° - 35° , 40° - 55° , and 60° - 85° . Therefore, one of the laboratory landslides in each of those three intervals of slope angles was chosen to show the snapshots during the whole motion. Figure 8 showed the snapshots of the laboratory landslides at 30° , 50° , and 80° . At 30° , the sliding mass slid as a thin but uniform form with a wide distribution on the inclined plate. The distribution width was almost a constant (Figure 8 (a)). At 50° , the sliding mass was a fan-shaped distribution and expanded on the inclined plate with the time after release. The sliding mass had an uneven thickness with concentrated sand on its surface. The concentrated sand was mainly distributed in the centreline of the sliding mass and the thickness of the sliding mass decreased continuously across to the flanks (Figure 8 (b)). At 80° , the fan-shaped expansion on the inclined plate lessened. The thickness distribution of the sliding mass on the inclined plate was very uneven and the motion was like freely-falling (Figure 8 (c)). There was a front thin layer formed in front of the main deposit at 80° and 85° .



(a)



(b)

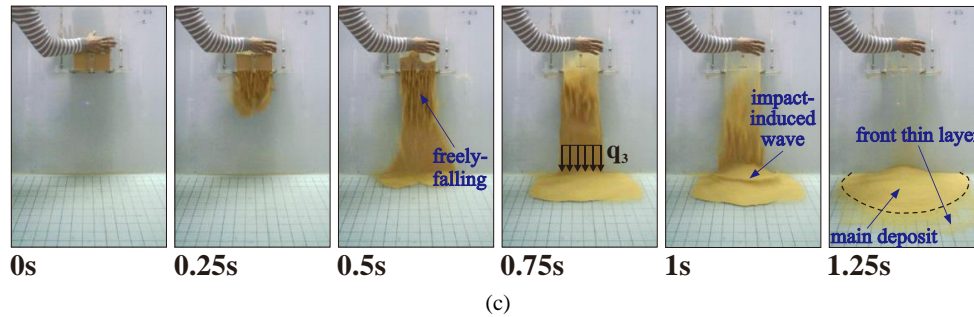
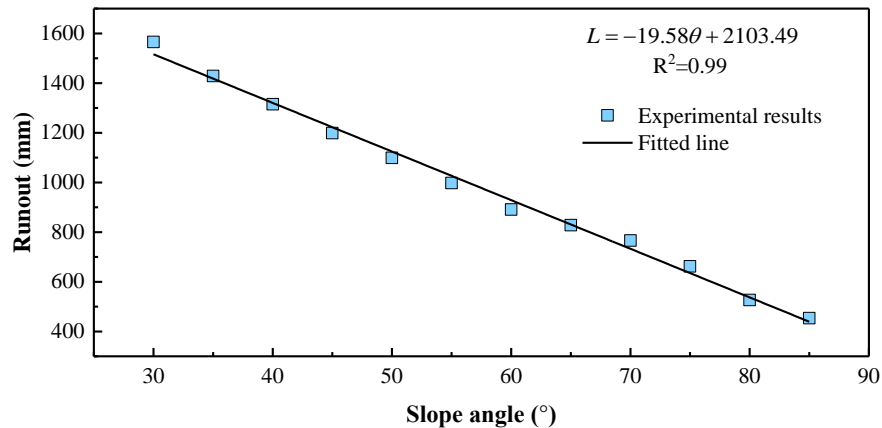


Figure 8. Movement processes of the laboratory landslides at slope angles of (a) 30°; (b) 50° and (c) 80°.



230 Figure 9. Runout of the laboratory landslides at different slope angles.

Figure 9 shows the relations of the runout and length of slope for the laboratory landslides with slope angles. The runout was a horizontal projected length that was calculated from the most rear part of the sandbox to the front of the deposit. At 80° and 85°, that was from the most rear part of the sandbox to the front of the main deposit. When the slope angle increased from 30° to 85°, the runout decreased from 1565.67 mm to 453.8 mm. The runout (L) (figure 9) of these laboratory landslides decreased linearly with the increase of the slope angle (θ). The linear equation of the runout of the laboratory landslides can be expressed as:

$$L = -19.58\theta + 2103.49.$$

3.2.2 Dynamical parameters

The displacements of the laboratory landslides were calculated as the difference between the front position of the sliding mass and the starting point, which was the bottom of the sandbox (displacement = 0). The curve of displacement with time (Figure 10) shows that the displacement tended to increase in three stages: exponentially in the early stage, linearly in the middle stage, and logarithmically in the late stage. The inset of Figure 10 depicted the relation between the duration of the laboratory landslides and the slope angle. The duration of these laboratory landslides, which was the moment the front of the sliding mass ended moving, decreased with the increase of the slope angle in general. The points in time that the laboratory landslides encountered the slope break at 30°, 35°, 40°-45°, 50°-60°, 65°-85° were 1s, 0.75s, 0.625s, 0.5s, and 0.375s, respectively. The displacement decreased from 1613.29 mm to 1104.73 mm as the slope angle increased from 30° to 75°. At nearly vertical slope angles of 80° and 85°, the displacements were 1126.13 mm and 1340.71 mm, respectively.

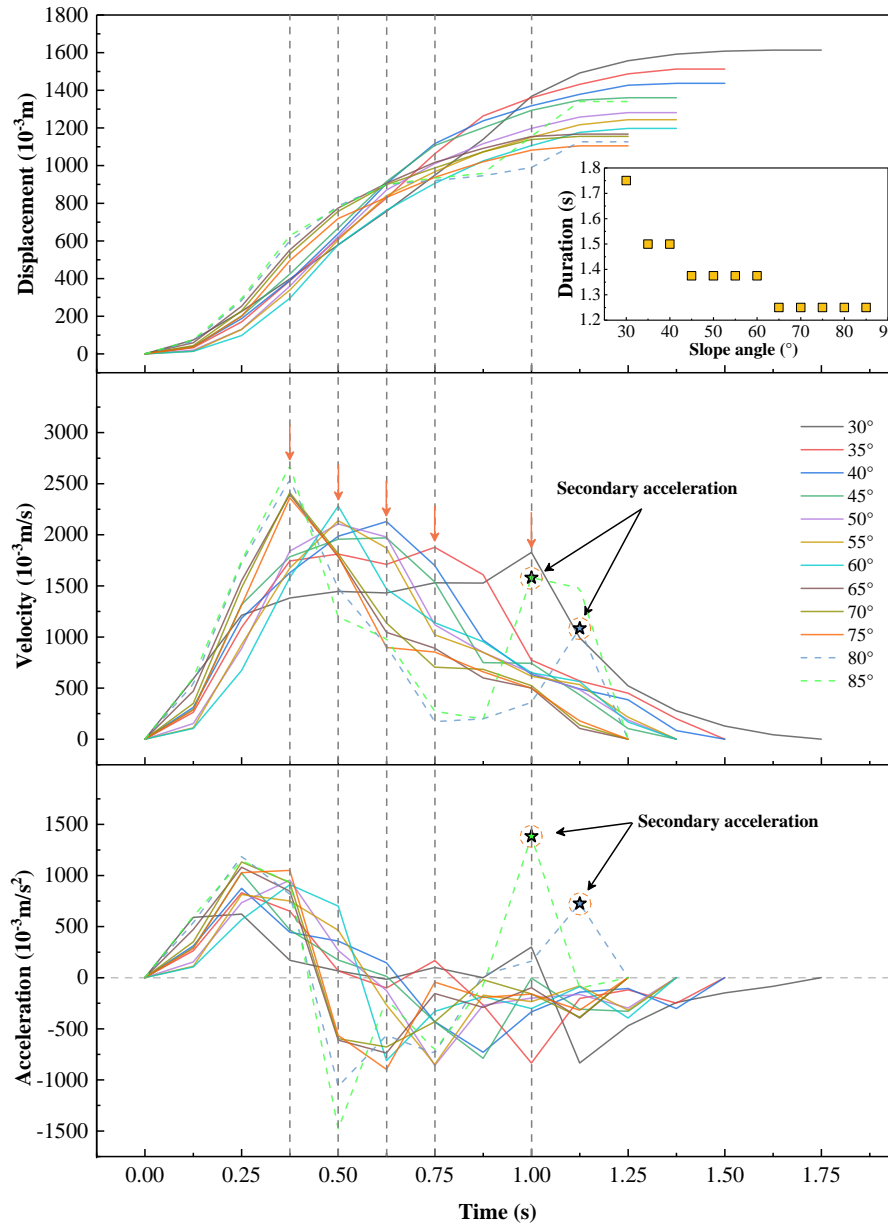


Figure 10. Curves of dynamical parameters with time for laboratory landslides at different slope angles: displacement-time curves (the inset is the relation between the duration of the laboratory landslides and the slope angle); velocity-time curves (the orange arrows represent the moment the sliding mass arrives at the slope break); acceleration-time curves.

The velocity of the laboratory landslides had three stages at low slope angles of 30° and 35°: uniform acceleration, constant-velocity, and deceleration. At 30°, these stages lasted 0.25 s, 0.75 s and 0.75 s, respectively; at 35°, they lasted 0.375 s, 0.5 s and 0.625 s. The first two stages were before the sliding mass encountered the slope break. According to the velocity curves, at moderate slope angles of 40°, 45°, 50° and 55°, the acceleration stage, which was before the sliding mass encountered the slope break, could be divided into a uniform acceleration stage and an acceleration stage at a decreasing rate. The acceleration stage at a



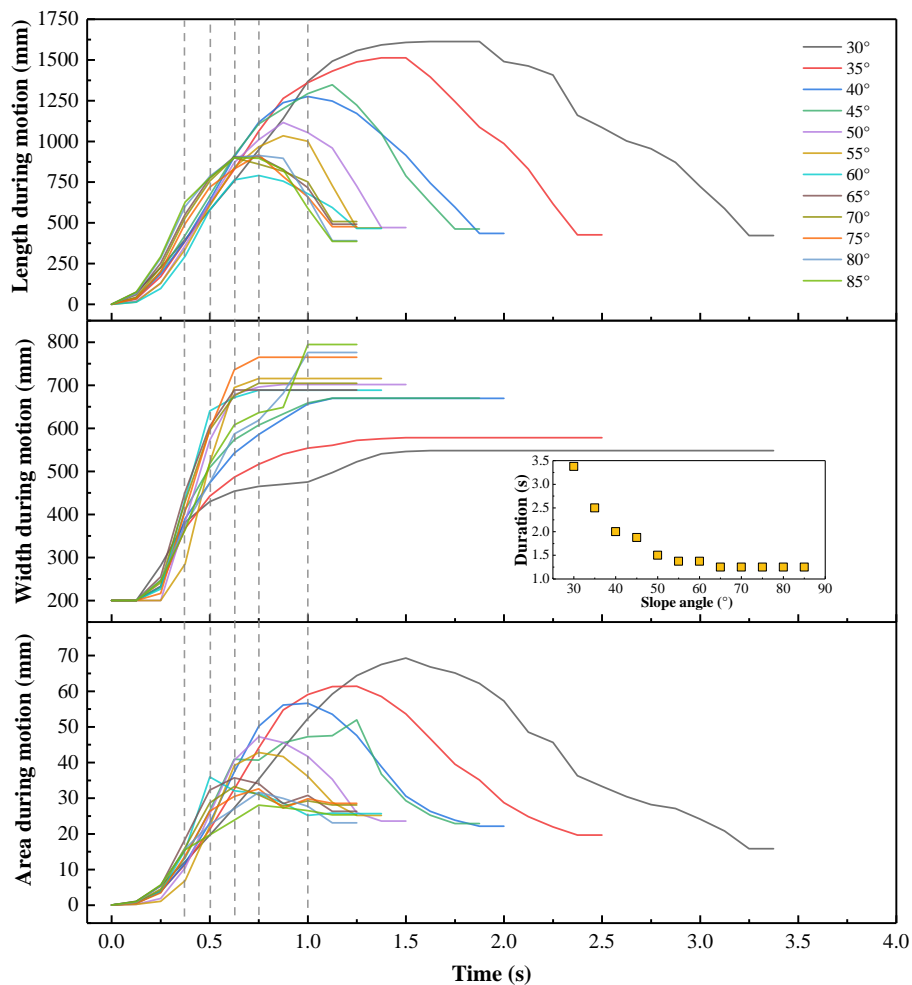
decreasing rate was unobvious, but still could be discerned. At high slope angles of 60°, 65°, 70°, 75°, 80°, and 85°, the laboratory landslides reached their peak velocity during the uniform acceleration stage, then immediately entered the deceleration stage. These laboratory landslides entered the deceleration stage after reaching their peak velocity when the front of the sliding mass encountered the slope break. However, at slope angles of 80° and 85°, a secondary acceleration occurred in the deceleration stage. The acceleration increased and decreased alternately, which indicates that the internal forces of the laboratory landslides increased and decreased alternately. The experiments were designed to have a constant potential energy so that the length of slope decreased as the slope angle increased. At slope angles of 30° and 35°, the length of slope was long and accordingly the front of the sliding masses tended to reach a steady velocity when sliding on the inclined plate. Nevertheless, for slope angles larger than 35° the front of sliding masses did not reach a steady velocity when sliding on the inclined plate regardless of the slope length.

After a comparison of the velocity curves (figure 10) and the motion processes (figure 8) of the laboratory landslides at different slope angles, the laboratory landslides would perform different motion characteristics. At low slope angles, the laboratory landslide had a thin and even thickness in the propagation range when sliding on the inclined plate. The velocity of the laboratory landslides comprised three stages: uniform acceleration, constant-velocity, and deceleration. At moderate slope angles, the laboratory landslide was uneven in thickness and fan-shaped when sliding on the inclined plate. The velocity also comprised three stages: uniform acceleration, acceleration at a decreasing rate, and deceleration. At high slope angles, the laboratory landslide was freely-falling when sliding on inclined plate. The velocity only comprised two stages: uniform acceleration and deceleration.

3.2.3 Morphological variations during the whole motion

The length of the laboratory landslides during motion was the difference from the most rear edge to the front of the sliding mass. The length of these laboratory landslides tended to increase in three stages: exponentially in the early stage, linearly in the middle stage, and logarithmically in the late stage. After reaching the maximum length during motion, the length of the sliding masses started to decrease. The increasing rate of the length at moderate and high slope angles was larger than that at small slope angles because the slope at moderate and high slope angles was larger. The maximum length of the laboratory landslides decreased in general with slope angles but increased at 45°. In addition, the maximum length for the laboratory landslides performed under slope angles of larger than 60° closed to a constant of 900mm, which was larger than that at 60° (figure 11). The gray dashed lines in figure 11 showed the moment the sliding mass arrived at the slope break. The points in time that the laboratory landslides encountered the slope break at 30°, 35°, 40°-45°, 50°-60°, 65°-85° were 1s, 0.75s, 0.625s, 0.5s, and 0.375s, respectively.

The width of the sliding mass during the motion of each laboratory landslide can be regarded as three stages. At the first stage, the width for most of the laboratory landslides was 200mm before 0.125s but before 0.25s for those at 50° and 55°, which was equal to the width of the sandbox. At the second stage, the width increased to the maximum width (namely maximum deposit width) with a rapidly increasing rate at 50° to 75°, but with a relatively low increasing rate at the other slope angles in this study. At the third stage, the sliding mass reached the maximum width and moved forward with this width (figure 11). The inset of Figure 11 depicted the relation between the duration of the laboratory landslides and the slope angle. The duration, which was the whole motion process of a laboratory landslide ended, decreased exponentially with the increase of the slope angle.



290 **Figure 11. Relations between the morphological parameters of the sliding masses during motion and time at different slope**
angles: length-time curve; width-time curve (the inset is the relation between the duration of the laboratory landslides and
the slope angle); and area-time curve.

The area of the sliding mass during motion showed a similar trend to that of the length. Most of the area during motion
 tended to increase to their maximum value in three stages: exponentially in the early stage, linearly in the middle stage, and
 295 logarithmically in the late stage. Nevertheless, at 60° the area increased to its maximum value exponentially. When these laboratory
 landslides reached to their maximum area during motion they started to decrease. The decreasing rate at slope angles of smaller
 than 60° was obviously larger than that at the other slope angles of this study because the slope at smaller than 60° was larger.
 Besides, the maximum area of these laboratory landslides during motion decreased with the increase of slope angles (figure 11).



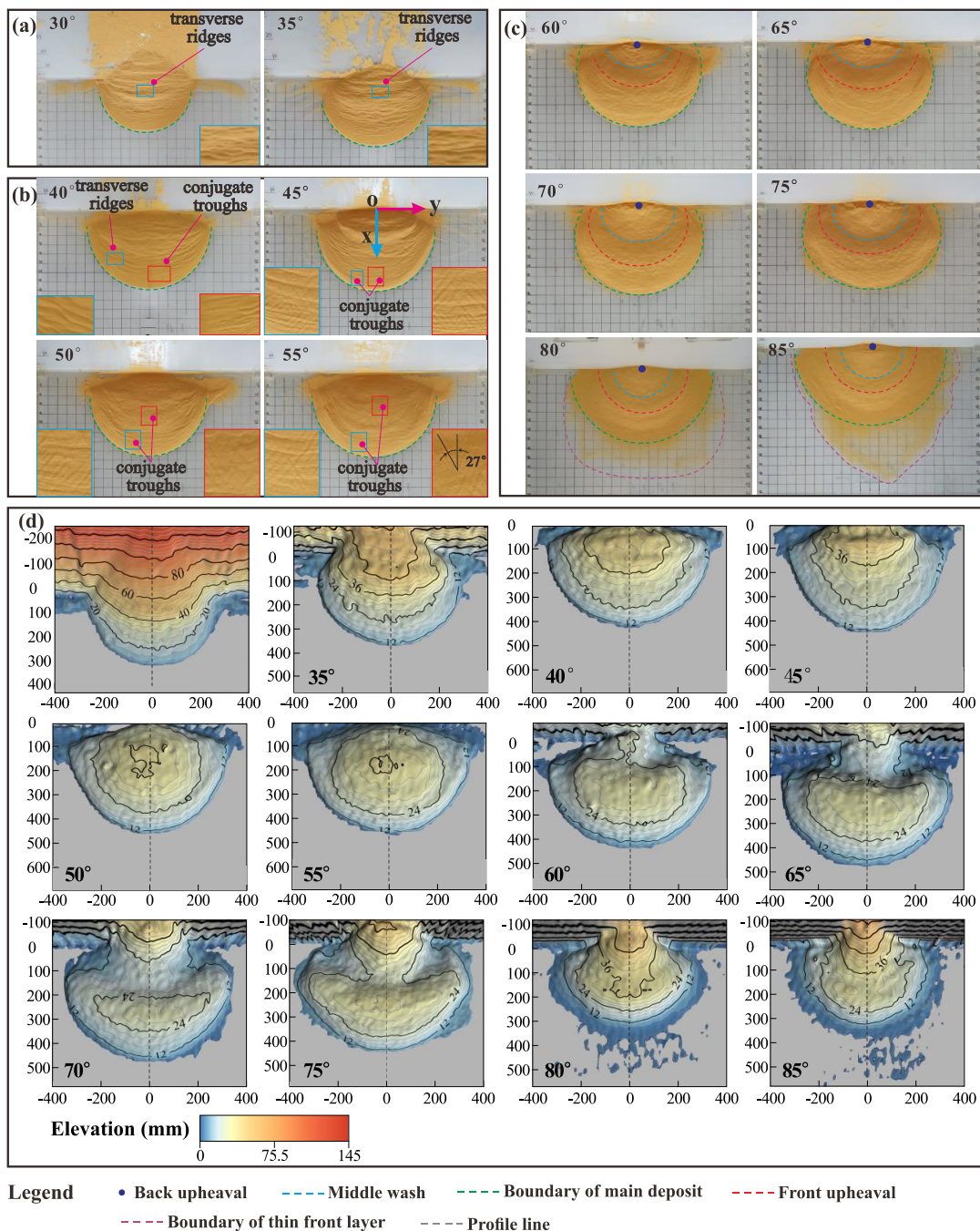
3.3 Deposit morphology

300 3.3.1 Deposit surface structures

To some extent, the surface morphology of a deposit can reflect the stress state of a landslide during its motion. Figure 12 (a) shows that transverse ridges were widely developed on the surfaces of deposits at low slope angles. The transverse ridges on the middle of the deposits were perpendicular to the motion direction (x axis direction) of laboratory landslides but with an acute angle to the x axis direction on the flanks of the deposits. The maximum acute angles between the transverse ridges on the flanks and x axis were 61° and 56° at slope angles of 30° and 35° , respectively. There was a denser distribution of transverse ridges on the flanks of the deposits comparing with that on the middle of the deposits not only at low slope angles but also moderate slope angles. The front boundaries of the deposits were tongue-like and part of the deposits leaned against the inclined plate.

Figure 12(b) shows the surface characteristics of deposits at moderate slope angles. Conjugate troughs (a kind of surface structures with X-shape wash) (figure 13) were widely formed on the deposit surfaces while transverse ridges lessened gradually with the increase of slope angles and were mainly distributed on the flanks of the deposits. Especially at 50° and 55° , transverse ridges were only discerned on the flanks of the deposits and not observed on the middle part of the deposits. At moderate slope angles, the conjugate troughs were only distributed on the front middle part of the deposits but extended backward when slope angles increased. The transverse ridges occurred at an angle to the motion direction (x axis direction). The angle got sharper with the increase of slope angles. At slope angles of 40° , 45° , 50° , and 55° , the maximum acute angles between the transverse ridges on flanks and x axis decreased and were 46° , 41° , 27° , and 15° , respectively. Like at low slope angles, the front boundaries of these deposits were tongue-like. At the slope angle of 40° , no deposits leaned against the inclined plate. In addition, besides the widely developed transverse ridges, rudimentary conjugate troughs were formed on the surface.

Figure 12 (c) shows that neither conjugate troughs nor transverse ridges were observed on the surfaces of deposits, but there were clear wave-like shapes. The wave-like shapes were also observed in the study of Roche et al. (2011b). Furthermore, at high slope angles, the surfaces were characterized by a double-upheaval with a wash area in-between. The front upheaval and back upheaval were with a relatively high elevation, but the middle wash was with a relatively low elevation. The double-upheaval was easier to discern by combining the images of the deposits at large slope angles (figure 12(c)) and their corresponding contour maps (figure 12(d)). At slope angles of 60° , 65° , 70° and 75° , the front boundaries of the deposits appeared round. At slope angles of 80° and 85° , the boundaries of the main deposits were round, with the front areas forming thin layers due to the impacting of later sliding mass (Penna et al., 2020; Morrissey et al., 1999). At these two slope angles, the deposits were consisted of two parts that were the main deposit and a thin front layer. Generally, with increases in slope angle, the rear boundaries of the deposits changed gradually from conical to straight, while the front boundaries changed gradually from tongue-like to round.



330 **Figure 12.** Surface morphologies of laboratory landslide deposits at various slope angles: (a) low slope angles; (b) moderate slope angles; (c) high slope angles, and (d) contour maps. The length of grid in horizontal plate is 5cm.

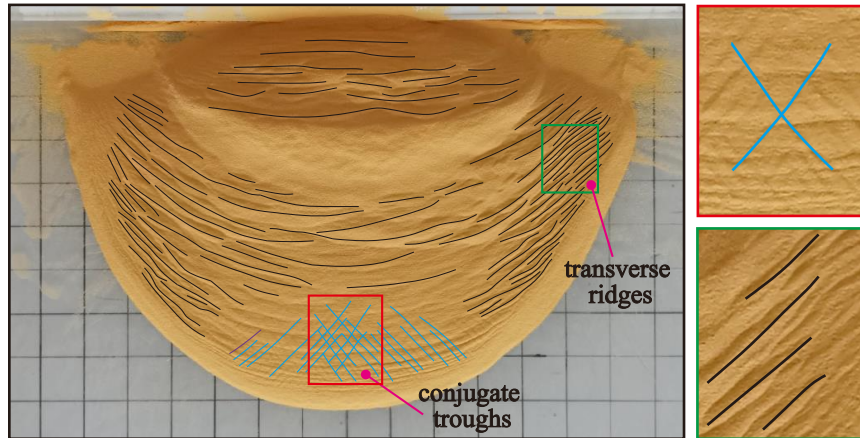
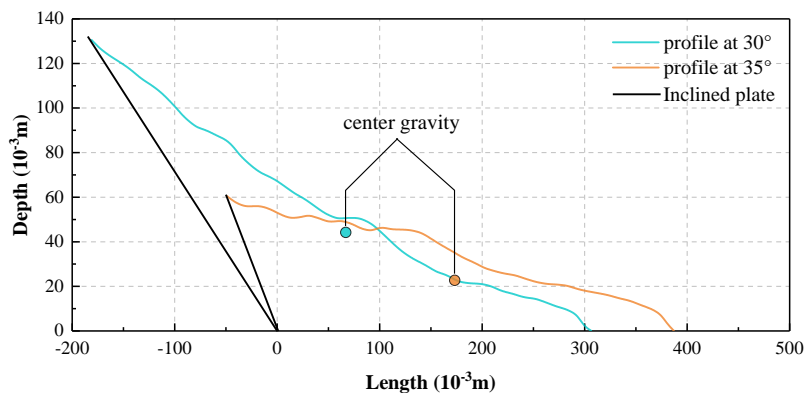


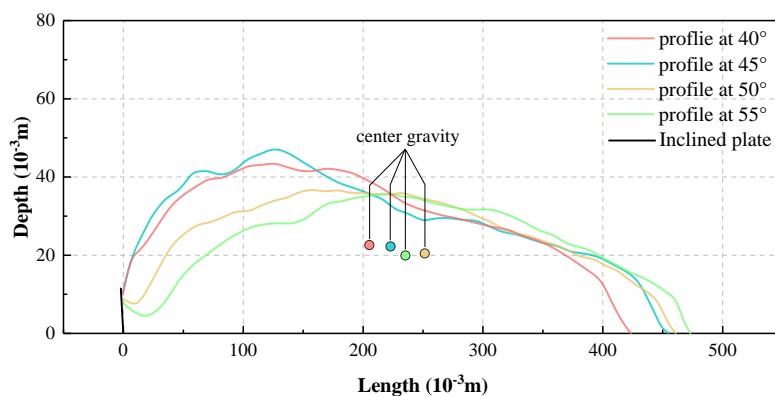
Figure 13. Transverse ridges and conjugate troughs at 45°.

3.3.2 Profile characteristics

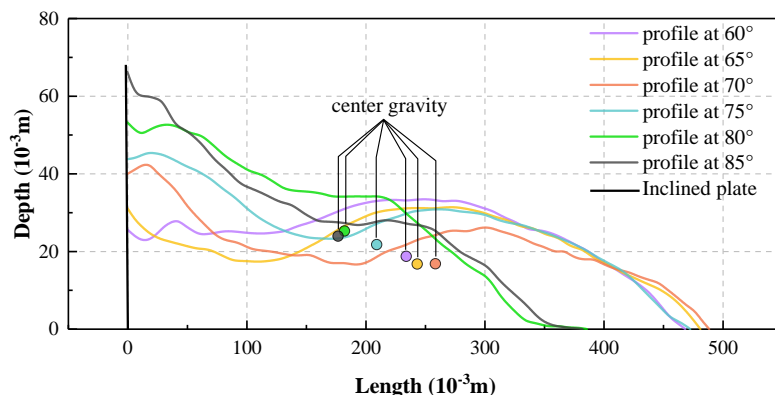
Figure 14 shows the profile morphologies of deposits formed at different slope angles. The profile locations correspond to the black dashed lines in Figure 13(d). Figure 14 (a) shows that the deposit profiles had a single-upheaval morphology at low slope angles, and the centre of gravity position decreased and moved forward with increases in slope angle. The front position of the deposits increased from 306.54 mm to 378.23 mm as the slope angle increased from 30° to 35°. In Figure 14 (b), the profile also has a single-upheaval morphology at moderate slope angles; the centre of gravity position moved forward first and then backward with increases in slope angle, while the height of the centre of gravity decreased. The front position of the deposits increased from 423.55 mm to 473.35 mm as the slope angle increased from 40° to 55°. Figure 14 (c) shows that the deposit profile at high slope angles presented a double-upheaval characteristic, which is clearly visible in Figure 12 (c) and (d). The centre of gravity position of the deposits moved forward with increases in slope angle and then backward at an angle of 70°. The height of the centre of gravity first decreased with increases in slope angle, then turned upward at 70° and, finally, decreased slightly at 85°. At 80° and 85°, there were the thin front layers, which was hard to display in the corresponding profiles. Therefore, the front position of the deposits in these two profiles was for the main deposit.



(a)



(b)



(c)

Figure 14. Profile morphologies of laboratory landslide deposits at different slope angles: (a) low slope angles; (b) moderate slope angles and (c) high slope angles.

3.3.3 Morphological parameters

355 In this paper, six parameters were used to describe the variations in deposit morphology according to slope angle:
 maximum length, maximum width, maximum depth, area, length-width ratio, and perimeter-area ratio. As aforementioned, the
 whole deposits were comprised of the main deposit and a thin front layer at 80° and 85°. Therefore, in figure 15 the variations of
 the main deposit and whole deposit were plotted for the maximum length, area, length-width ratio, and perimeter-area ratio. The
 length of these deposits was the horizontal projected distance from the most rear position of the deposits to the front. Figure 15 (a)
 360 shows that with the increase of slope angles the maximum length of the deposits decreased first but at 40° increased gradually for
 the whole deposit and increased sharply at 80° and 85°, while decreased for the main deposit at these two slope angles. Figure 15
 (b) shows that the maximum deposit width increased with slope angles in general. However, the changing range of the maximum
 width was relatively small at 40° to 70°. The maximum deposit depth decreased first and then increased at 65° (figure 15 (c)).
 Figure 15 (b) and Figure 15 (c) are only comprised of the whole deposit, which was because the maximum widths for the main
 365 deposit and the whole deposit were identical, similarly for the case of the maximum depths. The deposit area increased
 progressively with slope angles but increased sharply at 80° and 85° for the whole deposit (figure 15 (d)). However, it decreased
 in some extent at 80° and 85° for the main deposit. The deposit length-width ratio decreased generally with the slope angles for



the main deposit. Nevertheless, for the whole deposit it decreased first and then increased at 75°. The length-width ratio was no more than 1 (figure 15 (e)). The deposit perimeter-area ratio decreased generally with the slope angles for the main deposit and whole deposit, while increased at 40° and 70° (figure 15 (f)).

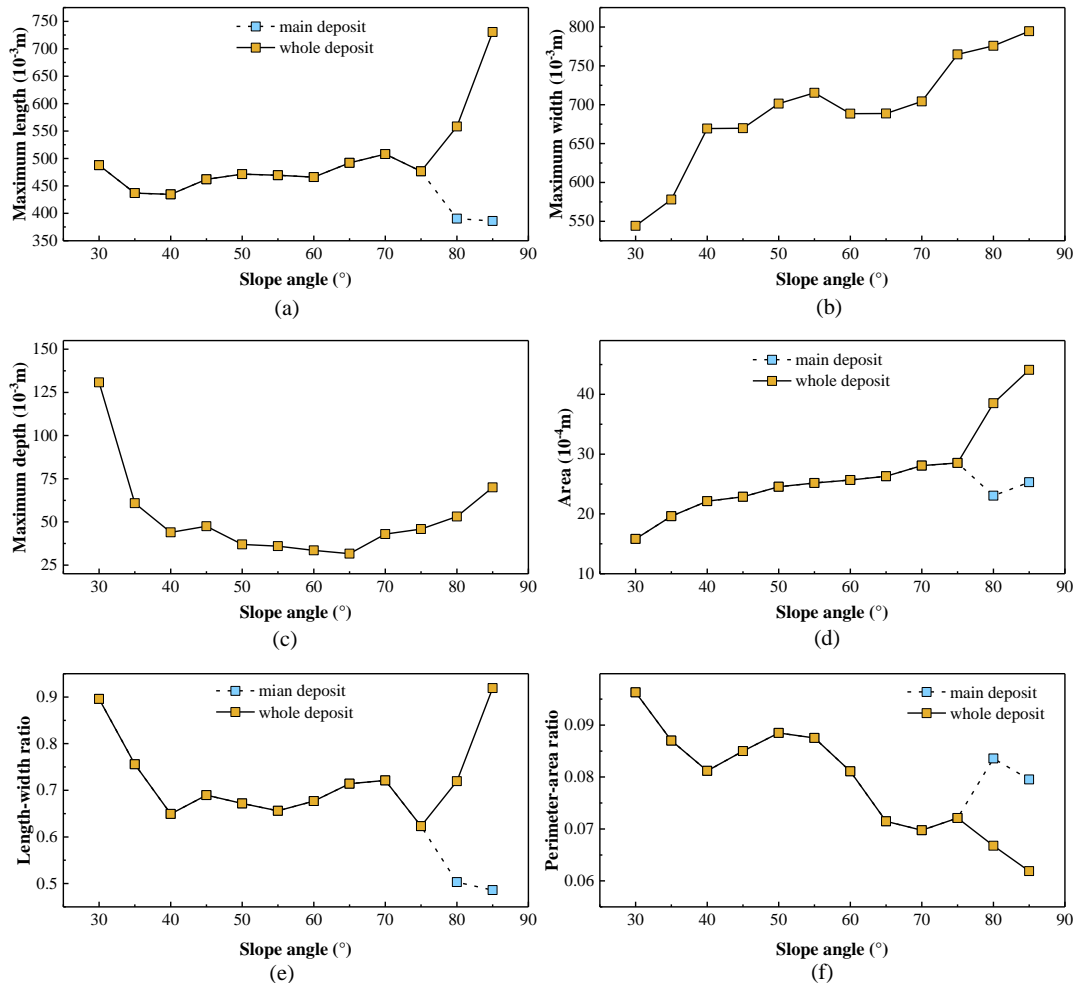


Figure 15. Laboratory landslide deposit morphology results (a) maximum length; (b) maximum width; (c) maximum depth; (d) area; (e) length-width ratio; and (f) perimeter-area ratio.

4 Discussion

375 4.1 Motion process

We noticed the differences in motion characteristics of the laboratory landslides. Here we will discuss how the velocity stages depend on the experimental apparatus and the implications of the morphological variations during the whole motion. In this study, the motion characteristic of laboratory landslides having three stages at low slope angles was observed, which is consistent with many previous studies (Cagnoli and Romano, 2012; Caccamo et al., 2012; Farin et al., 2014). Especially obvious was the



380 constant-velocity stage. Slope angles of 21° to 33° were considered in a study of the dynamic characteristics of laboratory landslides
by Caccamo et al. (2012), while slope angles of 0° to 24° were considered in a study on kinetic characteristics and deposit
morphologies by Farin et al. (2014). At these low slope angles, laboratory landslides would have the constant-velocity stage
although the experimental apparatus was installed with side walls in their studies. However, in a study by Hu et al. (2020) with a
slope angle of 40° (similar to the moderate slope angles in this paper) and side walls equipped with the experimental apparatus,
385 there was no the constant-velocity stage. Similarly, in experiments by Duan et al. (2021) at a slope angle of 60° without side walls
(similar to the high slope angles defined in this paper), there was also no the constant-velocity stage. From the above comparisons
with previous studies, the sliding mass showed a constant-velocity stage at low slope angles but no an obvious constant-velocity
stage at moderate and high slope angles, which indicated that the velocity stage characteristics of the sliding mass were less
dependent on experimental apparatuses (with or without side walls). Conversely, the slope angle is an important influence on the
390 motion state and velocity characteristics of landslides. At large slope angles, the velocities performed a sharp transition and were
less dependent on the slope angle, which was due to the particles was almost freely-falling at these slope angles. In this paper,
alternating increases and decreases in acceleration demonstrated stress fluctuations inside the laboratory landslides, which has
already been verified experimentally by Roche et al. (2021) and Bachelet et al. (2021).

At slope angles of 80° and 85° , a phenomenon of secondary acceleration could be discerned clearly in Figure 10. This
395 phenomenon is closely related to the waves formed during the motion of the sliding mass at these two slope angles (Figure 10).
Under the effect of the wave formed by the impact of the rear portion of the sliding mass, part of the deposit that had accumulated
on the horizontal plate would skip forward and move over the main deposit to form the thin frontal layer. The secondary
acceleration was generated during this process of impact and skipping.

The area of a landslide during motion reflects directly its influence range. The results indicated that the influence range
400 of a natural landslide moving on a broad and less restraining place was not infinite. During the motion of a landslide with an even
and broad motion path, the length and area would decrease under a constant volume after reaching the maximum length and area.
The continuous varying area for each laboratory landslide during the whole motion demonstrated that the average depth varied
during motion because the volume was constant. Consequently, the basal shear stress was changing during the whole motion. At
high slope angles, the area of these laboratory landslides during motion was less dependent on slope angles and time after they
405 reached their maximum areas because the sliding mass was freely-falling and less dependent on the slope angles.

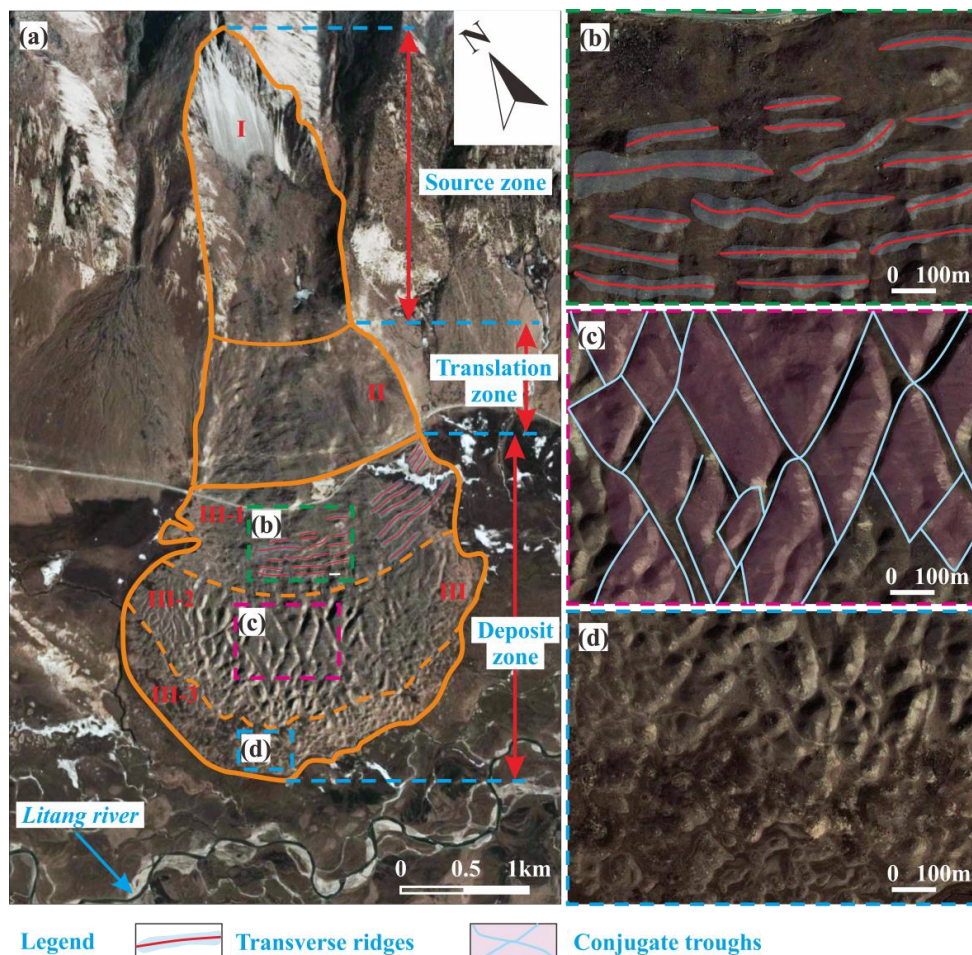
4.2 Surface morphology

In this paper, the motion process of the laboratory landslides differed at different slope angles. At low slope angles, the sliding
mass was slow and continuous sliding. At moderate slope angles, it was rapid lateral expansion sliding. At high slope angles, it
was impact skip sliding. Corresponding to these different motion processes, the surface and profile morphologies of the laboratory
410 landslide deposits also differed. The surface morphologies of transverse ridges, conjugate troughs, and double upheaval were
observed on the deposit surface of natural landslides. Hence, it is necessary to clarify the reason for the formation of these surface
morphologies from the insight of experiments.

At low slope angles, transverse ridges were distinct on the deposit surface (Figure 12 (a)). At moderate slope angles,
conjugate troughs developed widely across the deposit surface, while transverse ridges lessened gradually with the increase of
415 slope angles. This type of transverse ridge and conjugate trough morphology has been observed on the deposit surface of the
Luanshibao landslide (Tibet Plateau, Sichuan, China; Figure 16 (b) and (c)), which has a source area slope angle of 45° (Dai et al.,
2019). The transverse ridges on the middle part of the deposit are almost perpendicular to the motion direction of the landslide but



with an acute angle on the flanks of the deposit, which is consistent with this study. The formation of the transverse ridges is closely related to the stress state, which was like that of a thrust structure in which there is resistance at the front and thrust at the back acting mutually on the sliding mass (Wang et al., 2018b; Zhao et al., 2021; Crosta et al., 2017). The deflexion of transverse ridges on the flanks demonstrated the variations of the velocity of the sliding mass, which was in not only magnitude but also direction. The closer to the two sides was the sliding mass, the smaller would be the velocity and the more deflexion would be the velocity (Mangeny et al., 2007a). The deflexion of the transverse ridges may be also contributed to a lateral expansion of the sliding mass, in which the later sliding mass was obstructed by the front sliding mass and therefore had a tendency sliding towards the sides. During this process, the motion direction of the sliding mass closed to the sides changed. As a consequence, during the process of accumulation, the sliding mass closed to the sides would subject to compression and generate deflected transverse ridges on the flanks of the deposit. Wang et al. (2018b) and Zhao et al. (2021) proposed different mechanisms for the formation of conjugate troughs following in-situ investigations. Wang et al. (2018b) considered that conjugate troughs are formed by transport-parallel compression and radial spreading of the sliding mass. However, in Zhao et al. (2021), the formation of conjugate troughs was attributed to the stress state of the sliding mass during motion, which is similar to the triaxial stress state. Under this stress state, conjugate troughs are prone to develop in the deposit. To analyse any of a micro-unit in the deposit under moderate slope angles, according to the Mohr-Coulomb criterion, a pair of conjugate shear planes will be generated when the micro-unit reaches its ultimate failure stress under a pair of maximum principal stresses and a pair of minimum principal stresses caused by restriction at the two flanks. The angle between each plane and the maximum principal stress is $45^\circ - \varphi/2$. The internal friction angle φ of the sand used in the experiments was 36° . Therefore, based on the Mohr-Coulomb criterion, half of the angle between the conjugate shear planes was 27° . This angle is close to half of the acute angle between the conjugate troughs that was generated on the deposit surface in the experiments (Figure 12(b)). Therefore, the idea that conjugate troughs on the deposit surface are caused by shear behaviour is reasonable. The maximum principal stress σ_1 and minimum principal stress σ_3 causing shear behaviour occurred along and perpendicular to the direction of the sliding mass, respectively. In the study by Dai et al. (2019), the angle between the shear plane and maximum principal stress was 25° , which was calculated based on a deposit with an internal friction angle 40° . This angle is also close to half of the acute angle of about $20\text{--}25^\circ$ occurring between the conjugate troughs generated on the Luanshibao landslide's deposit surface. Hummocks are apparent in Figure 16 (d), which Dufresne and Davies (2009) consider to form due to the disintegration of a deposit caused by the velocity difference between the front and rear portions of the sliding mass. The present study prefers the explanation of Paguican et al. (2014) based on their experimental research and field investigations that the disintegration of a deposit causes hummocks; however, the cause of disintegration is shear in the vertical direction and conjugate shear. After disintegration, the sliding mass still moves forward and forms rudiments of hummocks. Subsequently, the hummocks are reinforced by weathering erosion. Wang et al. (2018b) proposed that the hummocks on the surface of the Luanshibao landslide's deposits were generated after radial propagation, based on the study by Paguican et al. (2014). The reason why the sliding mass spreads radially is because its bottom portion carries water during propagation.



450

Figure 16. Morphology of the Luanshibao landslide deposit in the Tibetan Plateau, Sichuan, China. (a) image of Luanshibao landslide (the base map is from © Google Earth); (b) transverse ridges; (c) conjugate troughs; (d) hummocks.

The double-upheaval morphology appeared on the surfaces of deposits at high slope angles, which is consistent with previous physical modelling studies (Roche et al., 2011a; Duan et al., 2020; Lajeunesse et al., 2005; Lajeunesse et al., 2006; Lajeunesse et al., 2004) and field investigations (Hutchinson, 2002; Quantin et al., 2004). This morphology was observed by Roche et al. (2011a) in a cylinder experiment (where sand was filled into a cylinder that was lifted up rapidly to release the sand), who proposed that it is caused by the wave formed by the impact of later sand to the sand reached already on the horizontal plate. Once the sand was motionless, alternating crests and troughs were distributed across the surface of the deposit. The method used by Roche et al. (2011a)—of lifting a cylinder upward to allow sand to collapse and move—is similar to the present study’s method of releasing sand from a box above a high-angled slope. In this study, when a laboratory landslide was released and started to slide in a way of freely-falling, the later portion of the sliding mass would impact the portion that was already static on the horizontal plate. This caused the static part to surge forward and form waves on its surface. To consider together the wave formed during motion of the sliding mass and the morphology of double-upheaval, when the wave formed on the surface of the deposit was to slow down and deposit, the crest and trough developed gradually into the front upheaval and middle wash, respectively, and the impact mass (rear portion of the sliding mass) was deposited at the slope break to form back upheaval. Certainly, the formation of

455

460

465

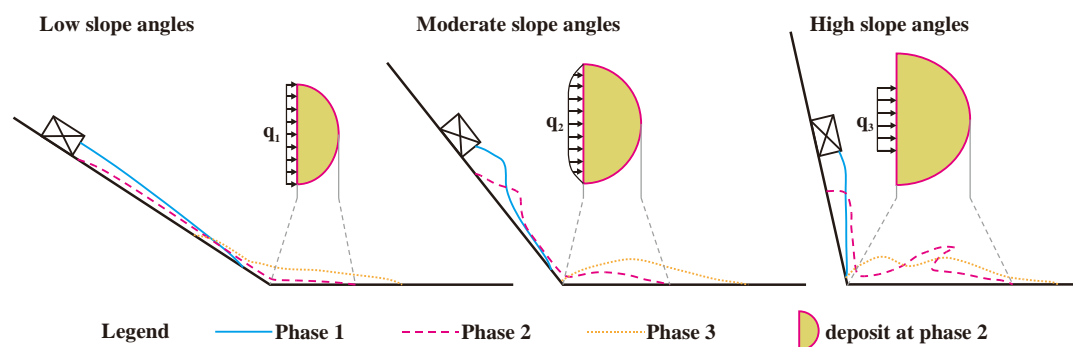


the double-upheaval may also be due to a relative motion in the sliding mass. The faster sliding particles arrived at the horizontal plate were stacked by the succeeding mass of slower moving particles, for which the front upheaval was formed. For the obstruction of the front upheaval, part of sliding mass deposited at rear of the front upheaval to form the middle wash. The most slower moving particles accumulated at the slope break coming into being the back upheaval. For the latter cause of the double-upheaval, a gentle
470 accumulation process was needed (i.e. the accumulation process of the moving particles is slow and constant contact). Conversely, from the freely-falling motion form and impact-induced wave the accumulation process of the sliding mass was violent. In fact, we more inclined to that the double-upheaval is caused by the wave during motion of the sliding mass, which is supported by two aspects according to the experimental phenomena. The one was that the wave surged forward on the sliding mass were observed and also mentioned in studies of Mangeney et al. (2010b) and Edwards and Gray (2015). The other one was that the motion process
475 of the sliding mass was freely-falling and the interaction among particles was violent, which made a gentle accumulation impossible. Therefore, it was unsupported in this study that the formation of the front upheaval and middle wash was due to the faster sliding particles were stacked by a succeeding mass of slower moving particles.

4.3 The difference of motion process

Velocity, acceleration and deposit morphology are externally observable forms of landslide motion. In this paper, different
480 motion forms were discerned according to differences in these external characteristics. However, the internal mechanisms causing these differences require further discussion. Here we will analyse the internal mechanisms of these differences and how they were affected by the motion process of the sliding mass.

At low slope angles, the sliding mass slid as a thin but uniform form with a wide distribution on the inclined plate. Therefore, the force q_1 generated in the sliding mass at the slope break was low because of a broad distribution and large area
485 during motion but was evenly distributed and had a similar magnitude across the width of the deposit (Figs. 8 (a) and 17). In phase 2, the sliding mass on the horizontal plate slowed down. The sliding mass still flowing on the inclined plate produced low thrust, making conjugate shear in the sliding mass difficult and only producing local overthrusting due to compression. Under the effect of thrust, transverse ridges developed widely on the deposit surface and part of the deposit piled against the inclined plate. At low slope angles, the sliding mass was dense and the particles were constant contact with each other. In such a case, more energy was
490 dissipated through frictional-collisional (i.e. inertial) (Iverson, 1997) interactions. The resultant force of the sliding mass along the inclined plate was similar in magnitude to the resistance. Therefore, the sliding mass was in a state of force balance and, correspondingly, there was an obvious constant-velocity stage.



495 **Figure 17. The different motion forms and phases of the laboratory landslides. The sliding mass is flowing on inclined plate in phase 1, and on both inclined and horizontal plates in phase 2, and the process of motion is end.**



At moderate slope angles, the sliding mass was fan-shaped and expanded on the inclined plate with the time after release. The sliding mass had an uneven thickness with concentrated sand on its surface. The concentrated sand was mainly distributed in the centreline of the sliding mass and the thickness of the sliding mass decreased continuously across to the flanks. Compared with the low-angle condition, the resultant force of the sliding mass along the inclined plate was higher due to a decreased friction force and an increased component of gravitational force along the inclined plate. Correspondingly, the force q_2 increased at the slope break. Due to the effect of the concentrated sand, the thrust was higher in the centreline of the sliding mass and lower near the flanks (Figs. 8 (b) and 17). In phase 2, the portion of sliding mass on the inclined plate was still accelerating when the front portion was slowing down on the horizontal plate. Due to the concentration of sand on the surface of the sliding mass, the thrust at the slope break was higher and more concentrated in the centreline of the sliding mass, which caused conjugate shear in the sliding mass on the horizontal plate. At moderate slope angles, the resultant force of the sliding mass along the inclined plate was higher than the resistance. Therefore, the sliding mass was not in a state of force balance and, correspondingly, there was no obvious constant-velocity stage.

At high slope angles, the fan-shaped expansion on the inclined plate lessened with increases in slope angle. The thickness distribution of the sliding mass on the inclined plate was very uneven and the motion was freely-falling (Figure 8 (c)). Due to the motion form of the sliding mass was freely-falling (i.e. in a gaseous state) (Lube et al., 2020; Roche et al., 2016; Lajeunesse et al., 2004; Roche et al., 2010; Roche et al., 2011a), several particles sustained neither any inertial interactions with other particles nor with the inclined plate and hence incurred less energy loss. Compared with the moderate slope angle condition, the resultant force of the sliding mass along the inclined plate was higher further due to the motion form of the sliding mass was freely-falling which would decrease the friction force and increase the component of gravitational force along the inclined plate. Correspondingly, the force q_3 at the slope break was higher, which only acted on the centreline region of the deposit (Figs. 8 (c) and 17). At high slope angles, the resultant force of the sliding mass along the inclined plate was much higher than the resistance. Therefore, the sliding mass was not in a state of force balance and there was no constant-velocity stage. In phase 2, the sliding mass on the inclined plate impacted the deposit already accumulated on the horizontal plate, which formed a double-upheaval morphology as the sliding mass slowed down on the horizontal plate.

4.4 Apparent friction coefficient

The apparent friction coefficient is a dimensionless parameter that can reflect the mobility of landslides and is widely used in field investigations and physical modelling experiments (Bowman and Take, 2018; Scheevel, 2017; Mcdougall, 2016; Dufresne et al., 2021; Devoli et al., 2009; Legros, 2002). Many researchers have analysed the relationship between the apparent friction coefficient and slope angle based on field data (Hunter and Fell, 2003; Whittall et al., 2016; Okura et al., 2003; Lucas et al., 2014). However, the disadvantage of this method is that the geological environments of each landslide are different, so statistical results can be inconsistent. Hence, it can be advantageous to study this relationship by theoretical deduction. Pudasaini and Miller (2013) proposed an advanced model from the viewpoint of physical and rheological functions to study the relationship between the apparent friction coefficient and area of landslides. The advanced rheological function was taking into consideration of the volume, physical parameters, and topographic parameters of landslides. Crosta et al. (2015b) studied this relationship from the view of energy conversion and dissipation of landslides during their motion and derived a formula shown as follow:

$$H / L = \frac{\tan \theta}{1 + (\cos \theta + \varepsilon \sin \theta)^2 (\tan \theta / \mu - 1)} \quad (1)$$



Where H denotes the vertical drop of the laboratory landslide; L denotes the horizontal spread; θ is the slope angle; ε is a coefficient of restitution ($\varepsilon < 1$); and μ is the friction coefficient of the sand-plate interface.

This theoretical formula involves an important assumption—that after collision at the slope break, the horizontal velocity component of the sliding mass is totally converted into horizontal velocity. Meanwhile, the fraction of the vertical velocity component, with a coefficient ε , is converted into horizontal velocity. Both wood plates and plexiglass plates were used in physical modelling experiments by Crosta et al. (2015b). The Equation (1) was derived for cases not only with but also without erodible bed. For the two cases, the coefficient of restitution of the landslide and friction coefficient between the landslide and accumulation region were different. The coefficient of restitution would be smaller enough when the erodible bed existed on horizontal accumulation board but relatively large when there was no the erodible bed. The sand used in their experiments had a particle size range of 0.09–0.6 mm with an average particle size of 0.32 mm. The present study used plexiglass inclined and horizontal plates and sand with a particle size range of 0.014–0.6 mm and an average particle size of 0.18 mm. When the interfacial friction coefficient obtained in the present study was substituted into the theoretical formula Equation. (1) proposed by Crosta et al. (2015b), it did not reflect the experimental data well (Figure 18). In collision experiments, the rate of energy dissipation due to collision with a plane is exponentially related to the acute angle between the object's motion direction and the normal direction of the plane. The higher the angle, the greater the energy dissipation (Zhang et al., 2015; Ji et al., 2019; Wang et al., 2018a). Therefore, the theoretical relationship between the apparent friction coefficient and slope angle was re-deduced based on the experimental conclusion.

According to the law of conservation of energy:

$$\frac{1}{2}mv_i^2 = mgs_i \sin \theta - mg\mu s_i \cos \theta \quad (2)$$

Where s_i is the distance between the scarp of the sandbox and the slope break and v_i is the velocity of the sliding mass at the slope break.

According to the experimental research of Asteriou et al. (2012), Li et al. (2015) and Ji et al. (2019), the rate of energy dissipation due to collision with a plane is exponentially related to the acute angle between an object's motion direction and the normal direction of the plane. Therefore, the coefficient of energy dissipation is that the rate of energy dissipation divides 100. After a collision at the slope break, the coefficient of remaining energy is also exponentially related to the acute angle, which is $a^{b\theta}$. In consequence, it was assumed that the remaining energy in the sliding mass after a collision at the slope break is:

$$a^{b\theta} \frac{1}{2}mv_i^2 \quad (3)$$

In which a is < 1 ; b is an undetermined coefficient and is > 0 . and θ is also > 0 . These two parameters of a and b are introduced to construct the coefficient of remaining energy. There was more energy remaining in the sliding mass when a increased and b decreased.

Therefore, the displacement (s_h) on the horizontal plate can be calculated as:

$$s_h = \frac{a^{b\theta} v_i^2}{2g\mu} \quad (4)$$



The total sliding distance of the sliding mass is:

565
$$L = s_i \cos \theta + s_h \quad (5)$$

The height of the scarp of the sandbox to the horizontal plate is:

$$H = s_i \sin \theta \quad (6)$$

By combining Equations (2)-(6), the apparent friction coefficient is:

$$H / L = \frac{\tan \theta}{1 + a^{b\theta} (\tan \theta / \mu - 1)} \quad (7)$$

570 When a was constant at 0.945, b was 0.3 and μ was 0.42; then, a curve plotted according to Equation (7) reflects the
experimental data well. The friction coefficient 0.42 was a measured value using the direct shear tests in this study. To verify the
universality of Equation (7), it was compared with the experimental results of Crosta et al. (2017) and Crosta et al. (2015b) obtained
at conditions of the absence of an erodible layer. When a was constant at 0.945, b was 0.3 and μ was 0.57; then, the curve of
Equation (7) is also a good approximation of the experimental data of Crosta et al. (2017), who used wooden inclined and horizontal
575 plates and sand (particle size range = 0.09–0.6 mm, average particle size = 0.32 mm). Crosta et al. (2017) reported that the sliding
mass had difficulty sliding down a 30° slope, for which a friction coefficient μ of 0.57 was calculated. The experimental conditions
used by Crosta et al. (2017) and the present study were similar apart from the difference of the sand and inclined and horizontal
plate materials, which resulted in different friction coefficients. Therefore, the a and b were 0.95 and 0.3, respectively, which
were equal to those of present study. When a was constant at 0.945, $b = 0.3$ and $\mu = 0.5$ and the curve plotted using Equation (7)
580 could reflect well the data of Crosta et al. (2015b) when using plexiglass inclined and horizontal plates. However, Crosta et al.
(2015b) used the sand with a particle size range of 0.09–0.6 mm and an average particle size of 0.32 mm, which is larger than the
sand in present study. According to interfacial shear tests conducted by Kim and Ha (2014), the interfacial friction angle increases
with particle size. Therefore, the coefficient of the friction in Crosta et al. (2015b) should be large than 0.42 used in present study.
The interfacial friction coefficient of 0.57 between the sand and wood used in Crosta et al. (2017) should be large than the friction
585 coefficient between the sand and plexiglass used in Crosta et al. (2015b). Therefore, the coefficient of the friction between the sand
used by Crosta et al. (2015b) and plexiglass was set as 0.5, which was relatively reasonable between 0.42 and 0.57.

Although Equation (7) can approximate the experimental results of the present study and those of Crosta et al. (2017) and Crosta
et al. (2015b), it should also be compared with field data of landslides. Therefore, data on landslides with different lithologies and
from different regions were collected. Apparent friction coefficients and slope angles were collected from studies on landslides in
590 British Columbia, Canada (Hunter and Fell, 2003), landslides in Hong Kong, China (Whittall et al., 2016), and chalk flows on the
southern coast of northern Europe (Crosta et al., 2017). Referring to Crosta et al. (2015b), parameters μ and b in Equation (7) were
set different values respectively to compare and verify the distribution of these data of landslides. When a was constant at 0.945,
 $\mu = 0.15$ and 0.5, and $b = 0.4, 0.6,$ and 0.8, respectively, the curve in Figure 19 based on Equation (7) reflects the distributions of
these landslide data well. As a consequence, the formula can reflect the change trend between the apparent friction coefficient and
595 slope angle well. Moreover, the formula been set different values of μ and b can provide a value range of H/L for a natural landslide
if the slope angle is known but difficultly to provide an accurate value of H/L . Nevertheless, for laboratory landslides, the formula
can provide a relatively precise value of H/L when the slope angle and friction coefficient of materials are known.

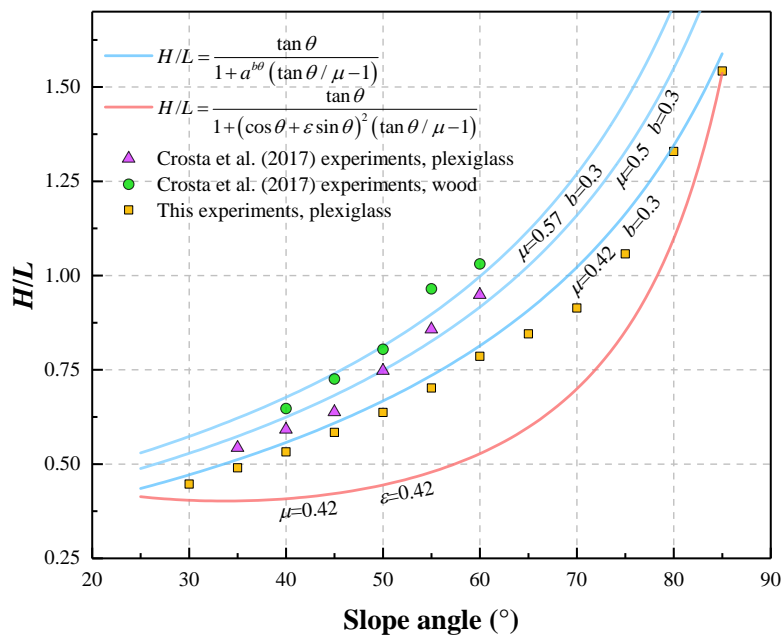


Figure 18. Relationships between the apparent friction coefficient of laboratory landslides and slope angle (μ is obtained by shear tests in this study).

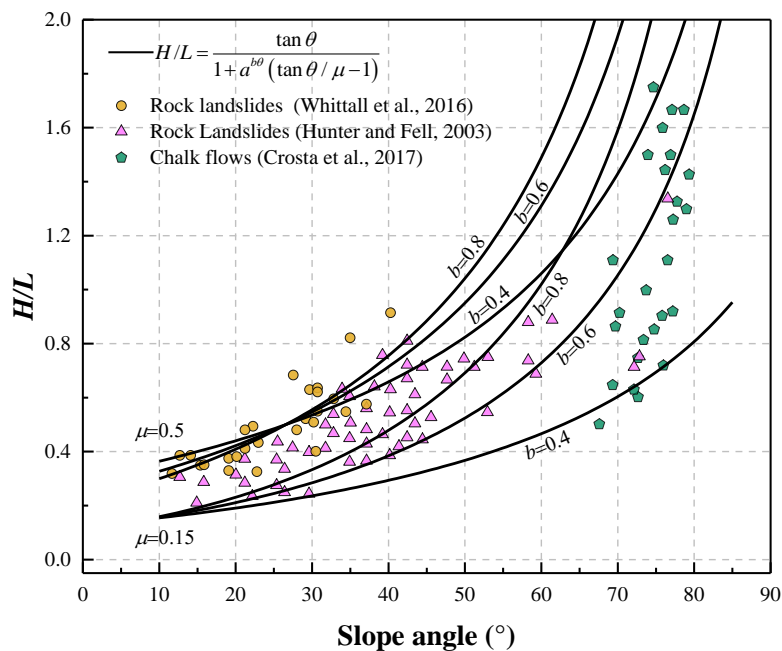


Figure 19. Relationships between the apparent friction coefficients of natural landslides and slope angle.



4.5 Runout of laboratory landslides

The runout of a landslide is closely related to the energy dissipation during the whole motion (Mangeny-Castelnaud et al., 2005). There are previous studies on the analysis of energy dissipation during the motion of landslides. In the study of Manzella and Labiouse (2013), they pointed out that the more angular and sharp was the slope break, the larger would be the energy dissipation and the shorter would be the travel distance. Similarly, the runout of the sliding mass decreased as the impact angle between an inclined chute and horizontal chute increased (Ge et al., 2020). Besides aforementioned studies on the runout by considering energy conversion, energy lines are often used to present the energy conversion and dissipation during the whole motion (Hung, 2006; Okura et al., 2000; Fan et al., 2016). Nevertheless, the shares of the amount of energy dissipation due to friction on the motion path and colliding at the slope break is unclear. The runout of the laboratory landslides was decreased almost linearly with the increase of the slope angles (Figure 9), which indicated that the total energy dissipation of the sliding mass increased linearly. What should be noticed was that the motion distance of the sliding mass slid on the inclined plate decreased with the increase of the slope angle when to control centre gravity height of the laboratory landslides was a constant of 0.7m. After an analysis of the force characteristics of the sliding mass, the larger the slope angle was, the lower the normal force acted on the inclined plate due to the sliding mass was. Correspondingly, the friction resistance of the sliding mass would decrease with the increase of the slope angle. Considering from the energy dissipation, the decrease of the motion distance and friction resistance would result in a lower energy dissipation when the slope angle increased. Therefore, the runout of the laboratory landslides should increase if only considering the energy dissipation caused by the friction resistance. Conversely, the runout decreased at the condition the initial potential energy was constant, which demonstrated that the amount of energy dissipation due to the collision of the sliding mass at the slope break was larger than that due to friction resistance. In fact, the amount of energy dissipation due to the friction resistance on the inclined plate can be expressed as:

$$E_f = \frac{H_c \mu mg \cos \theta}{\sin \theta} \quad (8)$$

Where H_c is the centre gravity height of the sandbox, μ is the friction coefficient of sand-plexiglass interface, m is the weight of the sliding mass, g is gravitational acceleration, θ is the slope angle.

The amount of energy dissipation due to the collision at the slope break is:

$$E_c = (1 - a^{b\theta}) \frac{1}{2} m v_i^2 = (1 - a^{b\theta}) mg H_c \quad (9)$$

The difference of E_f and E_c is:

$$E_f - E_c = \frac{H_c \mu mg \cos \theta}{\sin \theta} - H_c (1 - a^{b\theta}) mg = mg \left(\frac{H_c \mu \cos \theta}{\sin \theta} - H_c (1 - a^{b\theta}) \right) \quad (10)$$

Therefore,

$$\frac{(E_f - E_c)}{mg} = \frac{H_c \mu \cos \theta}{\sin \theta} - H_c (1 - a^{b\theta}) \quad (11)$$

Where the gravity mg is large than 0. Hence, $E_f - E_c > 0$ or < 0 is decided by $\frac{H_c \mu \cos \theta}{\sin \theta} - H_c (1 - a^{b\theta})$.

Figure 20 showed the change trend of $(E_f - E_c) / mg$, which was always < 0 at slope angles of 30° to 85° when the parameters



of $\mu = 0.42$, $a = 0.945$, and $b = 0.3$ were substituted into Equation 11. Correspondingly, $E_f - E_c$ was constantly larger than 0 at
 635 slope angles of 30° to 85° . In consequence, the runout of the laboratory landslides was more hinged on the slope angle compared
 with the motion distance of the sliding mass slid on the inclined plate.

Certainly, the longer runout of the laboratory landslides at lower slope angles may also attribute to the increase of
 accelerating distance due to the increase in the motion distance of the sliding mass slid on the inclined plate. Whether the decrease
 in the runout of the laboratory landslides owed to its decreased accelerating distance should be discussed further.

640

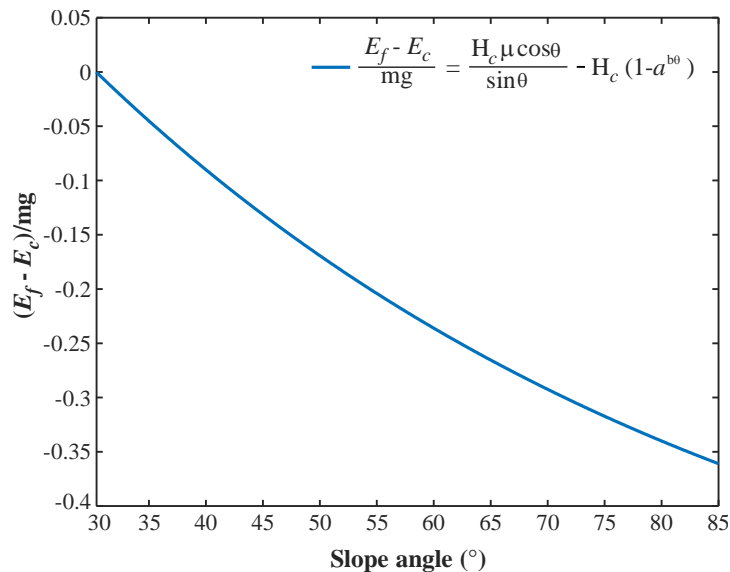


Figure 20. The difference of energy dissipation due to friction resistance and colliding at slope break with slope angle.

5 Conclusions

(1) Different motion characteristics of laboratory landslides were discerned at different slope angles. At low slope angles, their
 motion comprises three stages: uniform acceleration, constant-velocity, and deceleration. At moderate slope angles, their motion
 645 also comprises three stages: uniform acceleration, acceleration at a decreasing rate, and deceleration. At high slope angles, their
 motion only comprises two stages: uniform acceleration and deceleration. The runout of the laboratory landslides increased with
 the increase of slope angle, which means that the amount of energy dissipation is great due to a collision of the sliding mass at the
 slope break.

(2) The length and area of these laboratory landslides increase first and then decrease during their whole motion. The maximum
 650 area of these laboratory landslides during their whole motion decreases with the increase of slope angles. There is a maximum
 width to these laboratory landslides. After reaching the maximum width, the sliding mass will slide forward with this width.

(3) At low slope angles, transverse ridges are widely developed on the surface of the resulting deposit due to overthrusting caused
 by compression. At moderate slope angles, conjugate troughs formed by conjugate shear are observed on the surface. At high slope
 angles, the deposits exhibit a double-upheaval morphology because the rear portion of the sliding mass impacts the front portion



655 when it has already stopped and accumulated on the horizontal plate. This forms waves, the crests and troughs of which gradually develop into a frontal upheaval and a middle wash and the rear portion accumulates at the slope break to form the back upheaval.

(4) Under an assumption that the rate of energy dissipation after collision with a plane is exponentially related to the acute angle between the object's direction and the normal direction of the plane, a theoretical relationship between the apparent friction coefficient and slope angle was proposed. This formula provided good approximations of experimental data from this study and
660 others, as well as of field data on real landslides.

Availability of data and material

The data used to support the findings of this study are included in this paper.

Author contributions

Each author contributed to different parts, here listed: Conceptualisation: Yan-Bin Wu and Zhao Duan, Funding acquisition:
665 Zhao Duan, Conducting experiments and analysis: Yan-Bin Wu, Zhao Duan, Jian-Bing Peng, and Qing Zhang; Writing: Yan-Bin Wu and Zhao Duan.

Conflicts of interest

The authors declare that they have no known competing financial interests or personal relationships that could have appeared to influence the work reported in this paper.

670 Acknowledgments

This study would not have been possible without financial support from the Special Fund for the National Natural Science Foundation of China under Grant Nos. 42177155, 41790442, and 41702298. We thank the Team of Native English Editing (<https://www.nativeee.com>) for an English language editing.

References

- 675 Asteriou, P., Saroglou, H., and Tsiambaos, G.: Geotechnical and kinematic parameters affecting the coefficients of restitution for rock fall analysis, *International Journal of Rock Mechanics & Mining Sciences*, 54, 103-113, 10.1016/j.ijrmms.2012.05.029, 2012.
- Bachelet, V., Mangeney, A., Toussaint, R., DeRosny, J., Farin, M., and Hibert, C. J. a. p. a.: Acoustic emissions of nearly steady and uniform granular flows: a proxy for flow dynamics and velocity fluctuations, *JGR-Earth Surface*, 2021.
- 680 Baker, J., Gray, N., and Kokelaar, P.: Particle Size-Segregation and Spontaneous Levee Formation in Geophysical Granular Flows, *International Journal of Erosion Control Engineering*, 9, 174-178, 10.13101/ijece.9.174, 2016.



- Bowman, E. T. and Take, W. A.: TXT-tool 3.044-1.1: The Runout of Chalk Cliff Collapses—Case Studies and Physical Model Experiments, in: *Landslide Dynamics: ISDR-ICL Landslide Interactive Teaching Tools*, 297-314, 10.1007/978-3-319-57777-7_16, 2018.
- 685 Caccamo, P., Chanut, B., Faug, T., Bellot, H., and Naaim-Bouvet, F.: Small-scale tests to investigate the dynamics of finite-sized dry granular avalanches and forces on a wall-like obstacle, *Granular Matter*, 14, 577-587, 10.1007/s10035-012-0358-8, 2012.
- Cagnoli, B. and Romano, G. P.: Effects of flow volume and grain size on mobility of dry granular flows of angular rock fragments: A functional relationship of scaling parameters, *Journal of Geophysical Research: Solid Earth*, 117, n/a-n/a, 690 10.1029/2011jb008926, 2012.
- Crosta, G. B., Blasio, F. V. D., Locatelli, M., Imposimato, S., and Roddeman, D.: Landslides falling onto a shallow erodible substrate or water layer: an experimental and numerical approach, *IOP Conference Series: Earth and Environmental Science*, 26(1), 012004, <https://doi.org/10.1088/1755-1315/26/1/012004>, 2015a.
- 695 Crosta, G. B., Blasio, F. V. D., Locatelli, M., Imposimato, S., and Roddeman, D.: Landslides falling onto a shallow erodible substrate or water layer: an experimental and numerical approach, *IOP Conference Series: Earth and Environmental Science*, 10.1088/1755-1315/26/1/012004, 2015b.
- Crosta, G. B., Blasio, F. V. D., Caro, M. D., Volpi, G., Imposimato, S., and Roddeman, D.: Modes of propagation and deposition of granular flows onto an erodible substrate: experimental, analytical, and numerical study, *Landslides*, 14, 47–68, 10.1007/s10346-016-0697-3, 2017.
- 700 Dai, Z., Wang, F., Cheng, Q., Wang, Y., Yang, H., Lin, Q., Yan, K., Liu, F., and Li, K.: A giant historical landslide on the eastern margin of the Tibetan Plateau, *Bulletin of Engineering Geology and the Environment*, 78, 2055-2068, 10.1007/s10064-017-1226-x, 2019.
- Devoli, G., De Blasio, F. V., Elverhøi, A., and Høeg, K.: Statistical Analysis of Landslide Events in Central America and their Run-out Distance, *Geotechnical and Geological Engineering*, 27, 23-42, 10.1007/s10706-008-9209-0, 2009.
- 705 Duan, Z., Cheng, W.-C., Peng, J.-B., Rahman, M. M., and Tang, H.: Interactions of landslide deposit with terrace sediments: Perspectives from velocity of deposit movement and apparent friction angle, *Engineering Geology*, 280, 105913, <https://doi.org/10.1016/j.enggeo.2020.105913>, 2021.
- Duan, Z., Cheng, W. C., Peng, J. B., Wang, Q. Y., and Chen, W.: Investigation into the triggering mechanism of loess landslides in the south Jingyang platform, Shaanxi province, *Bulletin of Engineering Geology and the Environment*, 78, 4919-4930, 710 <https://doi.org/10.1007/s10064-018-01432-8>, 2019.
- Duan, Z., Wu, Y. B., Tang, H., Ma, J. Q., and Zhu, X. H.: An Analysis of Factors Affecting Flowslide Deposit Morphology Using Taguchi Method, *Advances in Civil Engineering*, 2020, 1-14, 10.1155/2020/8844722, 2020.
- Dufresne, A. and Davies, T. R.: Longitudinal ridges in mass movement deposits, *Geomorphology*, 105, 171-181, <https://doi.org/10.1016/j.geomorph.2008.09.009>, 2009.
- 715 Dufresne, A., Siebert, L., and Bernard, B.: Distribution and Geometric Parameters of Volcanic Debris Avalanche Deposits, in: *Volcanic Debris Avalanches: From Collapse to Hazard*, edited by: Roverato, M., Dufresne, A., and Procter, J., Springer International Publishing, Cham, 75-90, 10.1007/978-3-030-57411-6_4, 2021.
- Edwards, A. N. and Gray, J. M. N. T.: Erosion–deposition waves in shallow granular free-surface flows, *Journal of Fluid Mechanics*, 762, 35-67, 10.1017/jfm.2014.643, 2015.
- 720 Edwards, A. N., Viroulet, S., Johnson, C. G., and Gray, J. M. N. T.: Erosion-deposition dynamics and long distance propagation of granular avalanches, *Journal of Fluid Mechanics*, 915, A9, 10.1017/jfm.2021.34, 2021.



- Edwards, A. N., Viroulet, S., Kokelaar, B. P., and Gray, J. M. N. T.: Formation of levees, troughs and elevated channels by avalanches on erodible slopes, *Journal of Fluid Mechanics*, 823, 278-315, 10.1017/jfm.2017.309, 2017.
- 725 Fan, X. y., Tian, S. j., and Zhang, Y. y.: Mass-front velocity of dry granular flows influenced by the angle of the slope to the runout plane and particle size gradation, *Journal of Mountain Science*, 13, 234-245, 10.1007/s11629-014-3396-3, 2016.
- Farin, M., Mangeney, A., and Roche, O.: Fundamental changes of granular flow dynamics, deposition, and erosion processes at high slope angles: Insights from laboratory experiments, *Journal of Geophysical Research: Earth Surface*, 119, 504-532, 10.1002/2013jf002750, 2014.
- 730 Ge, Y., Zhou, T., Tang, H., and Lin, Z.: Influence of the impact angle on the motion and deposition of granular flows, *Engineering Geology*, 275, 105746, 10.1016/j.enggeo.2020.105746, 2020.
- Gray, J. M. N. T., Wieland, M., and Hutter, K.: Gravity-driven free surface flow of granular avalanches over complex basal topography, *Proceedings of the Royal Society of London. Series A: Mathematical, Physical and Engineering Sciences*, 455, 1841-1874, 10.1098/rspa.1999.0383, 1999.
- 735 Hu, Y. X., Li, H. B., Qi, S. C., Fan, G., and Zhou, J. W.: Granular Effects on Depositional Processes of Debris Avalanches, *KSCE Journal of Civil Engineering*, 24, 1116-1127, <https://doi.org/10.1007/s12205-020-1555-3>, 2020.
- Huang, R. Q. and Liu, W. H.: In-situ test study of characteristics of rolling rock blocks based on orthogonal design, *Chinese Journal of Rock Mechanics Engineering Geology(in Chinese)*, 28, 882-891, 2009.
- Hungr, O.: ROCK AVALANCHE OCCURRENCE, PROCESS AND MODELLING, *Landslides from Massive Rock Slope Failure*, Dordrecht, 2006//, 243-266.
- 740 Hunter, G. and Fell, R.: Travel distance angle for "rapid" landslides in constructed and natural soil slopes, *Canadian Geotechnical Journal*, 40, 1123-1141, 10.1139/t03-061, 2003.
- Hutchinson, J. N.: Chalk flows from the coastal cliffs of northwest Europe, 10.1130/REG15-p257, 2002.
- Iverson, R. M.: The physics of debris flows, *Reviews of Geophysics*, 35, 245-296, 1997.
- 745 Ji, Z.-M., Chen, Z.-J., Niu, Q.-H., Wang, T.-J., Song, H., and Wang, T.-H.: Laboratory study on the influencing factors and their control for the coefficient of restitution during rockfall impacts, *Landslides*, 16, 1939-1963, 10.1007/s10346-019-01183-x, 2019.
- Kim, D. and Ha, S.: Effects of Particle Size on the Shear Behavior of Coarse Grained Soils Reinforced with Geogrid, *Materials (Basel, Switzerland)*, 7, 963-979, <https://doi.org/10.3390/ma7020963>, 2014.
- 750 Lajeunesse, E., Mangeney-Castelnau, A., and Vilotte, J.: Spreading of a granular mass on a horizontal plane, *Physics of Fluids*, 16, 2371-2381, 2004.
- Lajeunesse, E., Monnier, J. B., and Homsy, G. M.: Granular slumping on a horizontal surface, *Physics of Fluids*, 17, 103302, 10.1063/1.2087687, 2005.
- Lajeunesse, E., Quantin, C., Allemand, P., and Delacourt, C.: New insights on the runout of large landslides in the Valles-Marineris canyons, Mars, *Geophysical Research Letters*, 33, L04403, <https://doi.org/10.1029/2005GL025168>, 2006.
- 755 Legros, F.: The mobility of long-runout landslides, *Engineering Geology*, 63, 301-331, [https://doi.org/10.1016/S0013-7952\(01\)00090-4](https://doi.org/10.1016/S0013-7952(01)00090-4), 2002.
- Li, K., Wang, Y.-F., Lin, Q.-W., Cheng, Q.-G., and Wu, Y.: Experiments on granular flow behavior and deposit characteristics: implications for rock avalanche kinematics, *Landslides*, 10.1007/s10346-020-01607-z, 2021.
- 760 Li, L. P., Sun, S. Q., Li, S. C., Zhang, Q. Q., Hu, C., and Shi, S. S.: Coefficient of restitution and kinetic energy loss of rockfall impacts, *KSCE Journal of Civil Engineering*, 20, 2297-2307, 10.1007/s12205-015-0221-7, 2015.



- Lin, Q., Cheng, Q., Li, K., Xie, Y., and Wang, Y.: Contributions of Rock Mass Structure to the Emplacement of Fragmenting Rockfalls and Rockslides: Insights From Laboratory Experiments, *Journal of Geophysical Research: Solid Earth*, 125, e2019JB019296, <https://doi.org/10.1029/2019JB019296>, 2020.
- 765 Lube, G., Breard, E. C. P., Esposti-Ongaro, T., Dufek, J., and Brand, B.: Multiphase flow behaviour and hazard prediction of pyroclastic density currents, *Nature Reviews Earth & Environment*, 1, 348-365, 10.1038/s43017-020-0064-8, 2020.
- Lucas, A., Mangeny, A., and Ampuero, J. P.: Frictional velocity-weakening in landslides on earth and on other planetary bodies, *Nature communications*, 5, 1-9, 2014.
- Lusso, C., Bouchut, F., Ern, A., and Mangeny, A.: A free interface model for static/flowing dynamics in thin-layer flows of granular materials with yield: simple shear simulations and comparison with experiments, *Applied Sciences*, 7, 386, 10.3390/app7040386, 2017.
- 770 Ma, P. H., Peng, J. B., Wang, Q. Y., Duan, Z., Meng, Z. J., and Jianqi, Z.: Loess landslides on the South Jingyang Platform in Shaanxi Province, China, *Quarterly Journal of Engineering Geology and Hydrogeology*, 52, 547-556, <https://doi.org/10.1144/qjegh2018-115>, 2019.
- Mangeny-Castelnau, A., Bouchut, F., Vilotte, J. P., Lajeunesse, E., Aubertin, A., and Pirulli, M.: On the use of Saint Venant equations to simulate the spreading of a granular mass, *Journal of Geophysical Research: Solid Earth*, 110, B09103, 10.1029/2004jb003161, 2005.
- 775 Mangeny, A., Bouchut, F., Thomas, N., Vilotte, J. P., and Bristeau, M. O.: Numerical modeling of self-channeling granular flows and of their levee-channel deposits, *JOURNAL OF GEOPHYSICAL RESEARCH*, 112, F02017, 10.1029/2006JF000469, 2007a.
- 780 Mangeny, A., Tsimring, L. S., Volfson, D., Aranson, I. S., and Bouchut, F.: Avalanche mobility induced by the presence of an erodible bed and associated entrainment, *Geophysical Research Letters*, 34, L22401, <https://doi.org/10.1029/2007GL031348>, 2007b.
- Mangeny, A., Roche, O., Hungr, O., Mangold, N., Faccanoni, G., and Lucas, A.: Erosion and mobility in granular collapse over sloping beds, *Journal of Geophysical Research*, 115, 10.1029/2009jf001462, 2010a.
- 785 Mangeny, A., Roche, O., Hungr, O., Mangold, N., Faccanoni, G., and Lucas, A.: Erosion and mobility in granular collapse over sloping beds, *Journal of Geophysical Research*, 115, F03040, 10.1029/2009jf001462, 2010b.
- Manzella, I. and Labiouse, V.: Extension of the fringe projection method to measure shape and position of the centre of mass of granular flow deposit, 12th International Conference of the International Association for Computer Methods and Advances in Geomechanics, 4547-4554, 2008.
- 790 Manzella, I. and Labiouse, V.: Empirical and analytical analyses of laboratory granular flows to investigate rock avalanche propagation, *Landslides*, 10, 23-26, 10.1007/s10346-011-0313-5, 2013.
- McDougall, S.: 2014 Canadian Geotechnical Colloquium: Landslide runout analysis — current practice and challenges, *Canadian Geotechnical Journal*, 54, 605-620, 10.1139/cgj-2016-0104, 2016.
- Moro, F., Faug, T., Bellot, H., and Ousset, F.: Large mobility of dry snow avalanches: Insights from small-scale laboratory tests on granular avalanches of bidisperse materials, *Cold Regions Science and Technology*, 62, 55-66, <https://doi.org/10.1016/j.coldregions.2010.02.011>, 2010.
- 795 Morrissey, M. M., Savage, W. Z., and Wieczorek, G. F.: Air blasts generated by rockfall impacts: Analysis of the 1996 Happy Isles event in Yosemite National Park, *Journal of Geophysical Research B: Solid Earth*, 104, 23189-23198, 1999.
- Okura, Y., Kitahara, H., and Sammori, T.: Fluidization in dry landslides, *Engineering Geology*, 56, 347-360, [https://doi.org/10.1016/S0013-7952\(99\)00118-0](https://doi.org/10.1016/S0013-7952(99)00118-0), 2000.
- 800



- Okura, Y., Kitahara, H., Kawanami, A., and Kurokawa, U.: Topography and volume effects on travel distance of surface failure, *Engineering Geology*, 67, 243–254, [https://doi.org/10.1016/S0013-7952\(02\)00183-7](https://doi.org/10.1016/S0013-7952(02)00183-7), 2003.
- Paguican, E. M. R., van Wyk de Vries, B., and Lagmay, A. M. F.: Hummocks: how they form and how they evolve in rockslide-debris avalanches, *Landslides*, 11, 67–80, 10.1007/s10346-012-0368-y, 2014.
- 805 Parise, M.: Observation of surface features on an active landslide, and implications for understanding its history of movement, *Nat. Hazards Earth Syst. Sci.*, 3, 569–580, 10.5194/nhess-3-569-2003, 2003.
- Penna, I. M., Hermanns, R. L., Nicolet, P., Morken, O. A., and Jaboyedoff, M.: Airblasts caused by large slope collapses, *Geological Society of America Bulletin*, 2020.
- Petley, D. N.: Characterizing Giant Landslides, *Science*, 339, 1395, 10.1126/science.1236165, 2013.
- 810 Pirulli, M., Bristeau, M.-O., Mangeney, A., and Scavia, C.: The effect of the earth pressure coefficients on the runout of granular material, *Environmental Modelling & Software*, 22, 1437–1454, <https://doi.org/10.1016/j.envsoft.2006.06.006>, 2007.
- Pudasaini, S. P. and Miller, S. A.: The hypermobility of huge landslides and avalanches, *Engineering Geology*, 157, 124–132, <https://doi.org/10.1016/j.enggeo.2013.01.012>, 2013.
- Quantin, C., Allemand, P., and Delacourt, C.: Morphology and geometry of Valles Marineris landslides, *Planetary and Space*
815 *Science*, 52, 1011–1022, <https://doi.org/10.1016/j.pss.2004.07.016>, 2004.
- Roche, O., Buesch, D. C., and Valentine, G. A.: Slow-moving and far-travelled dense pyroclastic flows during the Peach Spring super-eruption, *Nature Communications*, 7, 10890, 10.1038/ncomms10890, 2016.
- Roche, O., Attali, M., Mangeney, A., and Lucas, A.: On the run-out distance of geophysical gravitational flows: Insight from fluidized granular collapse experiments, *Earth and Planetary Science Letters*, 311, 375–385, 10.1016/j.epsl.2011.09.023,
820 2011a.
- Roche, O., Attali, M., Mangeney, A., and Lucas, A.: On the run-out distance of geophysical gravitational flows: Insight from fluidized granular collapse experiments, *Earth Planetary Science Letters*, 311, 375–385, 2011b.
- Roche, O., Monserrat, S., Niño, Y., and Tamburrino, A.: Pore fluid pressure and internal kinematics of gravitational laboratory air-particle flows: Insights into the emplacement dynamics of pyroclastic flows, *Journal of Geophysical Research: Solid*
825 *Earth*, 115, B09206, <https://doi.org/10.1029/2009JB007133>, 2010.
- Roche, O., Wildenberg, S. v. d., Valance, A., Delannay, R., Mangeney, A., Corna, L., and Latchimy, T.: Experimental assessment of the effective friction at the base of granular chute flows on smooth incline, 2021.
- Scheevel, C. R.: Predicting landslide stability, runout, and failure velocity at Cook Lake landslide, Wyoming, Thesis Paper, Department of Geology and Geological Engineering, Colorado School of Mines, Colorado School of Mines, 2017.
- 830 Wang, Y., Jiang, W., Cheng, S., Song, P., and Mao, C.: Effects of the impact angle on the coefficient of restitution in rockfall analysis based on a medium-scale laboratory test, *Nat. Hazards Earth Syst. Sci.*, 18, 3045–3061, 10.5194/nhess-18-3045-2018, 2018a.
- Wang, Y. F., Cheng, Q. G., Lin, Q. W., Li, K., and Yang, H. F.: Insights into the kinematics and dynamics of the Luanshibao rock avalanche (Tibetan Plateau, China) based on its complex surface landforms, *Geomorphology*, 317, 170–183,
835 <https://doi.org/10.1016/j.geomorph.2018.05.025>, 2018b.
- Wei, Y., Xu, Q., Yang, H., Li, H., and Kou, P.: Dynamic Behavior and Deposit Features of Debris Avalanche in Model Tests Using High Speed Photogrammetry, *Sustainability*, 12, 10.3390/su12166578, 2020.
- Whittall, J., Eberhardt, E., and McDougall, S.: Runout analysis and mobility observations for large open pit slope failures, *Canadian Geotechnical Journal*, 54, 373–391, 10.1139/cgj-2016-0255, 2016.



- 840 Zeng, Q., Zhang, L., Davies, T., Yuan, G., Xue, X., Wei, R., Yin, Q., and Liao, L.: Morphology and inner structure of
Luanshibao rock avalanche in Litang, China and its implications for long-runout mechanisms, *Engineering Geology*, 260,
105216, <https://doi.org/10.1016/j.enggeo.2019.105216>, 2019.
- Zhang, G., Tang, H., Xiang, X., Murat, K., and Wu, J.: Theoretical study of rockfall impacts based on logistic curves,
International Journal of Rock Mechanics and Mining Sciences, 78, 133-143, <https://doi.org/10.1016/j.ijrmms.2015.06.001>,
845 2015.
- Zhao, B., Zhao, X., Zeng, L., Wang, S., and Du, Y.: The mechanisms of complex morphological features of a prehistorical
landslide on the eastern margin of the Qinghai-Tibetan Plateau, *Bulletin of Engineering Geology and the Environment*, 80,
3423-3437, 10.1007/s10064-021-02114-8, 2021.